

Phase transitions in water and glycerol under pressure

Temperature calibration and test measurements

by

Klara Holl

Bachelor thesis in physics
submitted to the Department of Physics, Mathematics and Computer Science
(FB 08)
of the Johannes Gutenberg-University Mainz
on August 07, 2023

1. Reviewer: Prof. Dr. Katrin Amann-Winkel
2. Reviewer: Prof. Dr. Jure Demsar

Phasenübergänge in Wasser und Glycerol unter Druck

Temperaturkalibrierung und Testmessungen

von

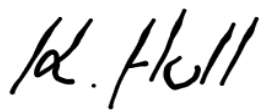
Klara Holl

Bachelorarbeit in Physik
vorgelegt dem Fachbereich Physik, Mathematik und Informatik (FB 08)
der Johannes Gutenberg-Universität Mainz
am 07. August 2023

1. Gutachterin: Prof. Dr. Katrin Amann-Winkel
2. Gutachter: Prof. Dr. Jure Demsar

I hereby declare that I have written the present thesis independently and without use of other than the indicated means. I also declare that to the best of my knowledge all passages taken from published and unpublished sources have been referenced.

Ich versichere, dass ich die Arbeit selbstständig verfasst und keine anderen als die angegebenen Quellen und Hilfsmittel benutzt sowie Zitate kenntlich gemacht habe.

A handwritten signature in black ink, appearing to read 'kl. Holl'.

Mainz, August 07, 2023

Klara Holl
KOMET
Institute of Physics
Staudingerweg 7
Johannes Gutenberg-University
D-55128 Mainz
klholl@students.uni-mainz.de

Zusammenfassung

Wasser ist allgegenwärtig, und dennoch bleibt es, durch seine vielen ungeklärten Eigenschaften, von großem wissenschaftlichen Interesse. Das komplexe Phasendiagramm zeigt zum heutigen Zeitpunkt neunzehn kristalline Phasen [8], die sich auch bei Raumtemperatur und durch hohen Druck formen lassen. Glycerol ist ebenso weit verbreitet und vor allem in Arzneimitteln und Lebensmitteln zu finden. In Verbindung mit Wasser ist die süße, viskose Flüssigkeit meist als Lösung in Frostschutzmittel bekannt.

Diese Arbeit beinhaltet Testmessungen für eine geplante Röntgen-Strahlzeit am DESY. Dort soll die Temperaturabhängigkeit des Glasübergangs und der Viskosität von Glycerol unter Zuhilfenahme von Gold-Nanopartikeln untersucht werden. Für diese Messungen wird im Rahmen dieser Arbeit eine Temperaturkalibrierung der Probenkammer durchgeführt. Dazu wird ein Thermoelement Typ K in das Cryostat an die Probe gebracht und der Temperatur-Offset zu einer sich ebenfalls im Cryostat befindlichen Si-Diode gemessen.

Des Weiteren werden Ramanmessungen zur Untersuchung des Phasenübergangs von Wasser zu Eis VI und Eis VII in einer symmetrischen Diamantstempelzelle durchgeführt. Mit Schrauben kann der Druck auf eine Probe im Inneren ausgeübt werden, der dann über die Fluoreszenz eines Rubin-Balls bestimmt wird. Auch werden Glycerollösungen im Bereich von 2 - 50 mol% hergestellt und Raman-Spektren aufgenommen.

Table of contents

1. Introduction	1
2. Scientific background	2
2.1. Phase transitions in water and ice	2
2.2. Glycerol	3
3. Experimental methods	6
3.1. The diamond anvil cell	6
3.1.1. Symmetric diamond anvil cell	6
3.1.2. Mounting the diamond on the seat	6
3.1.3. Aligning the diamonds in the cell	6
3.1.4. Preparing steel gaskets	7
3.1.5. Preparing a sample	8
3.2. Cryostat	8
3.2.1. Principles and operation of thermocouples and diodes	8
3.3. Raman spectroscopy	9
3.3.1. Ruby fluorescence	10
3.3.2. Raman scattering	11
3.4. Preparation of glycerol-water mixtures	12
4. Results of the temperature calibration	14
4.1. Cooling the cryostat with nitrogen	14
4.2. Heating the cryostat with the diode	15
5. Results of the Raman spectroscopy	18
5.1. Phase transitions of water at room temperature	18
5.1.1. Pressure determination	18
5.1.2. Water phase transition	19
5.1.3. Water and air bubble in DAC	22
5.2. Raman spectrum of pure glycerol	23
5.3. Raman spectra of glycerol-water mixtures	25
6. Summary and outlook	27
A. Appendix	28
A.1. Tables and figures	29
A.1.1. Sketches of components	29
A.1.2. Temperature calibration	32

Table of contents

A.2. Raman measurements	33
A.2.1. Ruby spectra	33
A.2.2. Glycerol mixtures	37
B. Bibliography	37
C. Acknowledgements	42

1. Introduction

Despite being one of the most used substances, water is of great scientific interest. It has several anomalous properties, many of which are still unknown to humanity. One of them is the density maximum at 4°C, or its solid state, ice, not sinking in liquid water. As of today, water has 19 known crystalline phases [8]. Glycerol is a substance used in various applications, for example, in pharmaceutical technologies or foodstuffs. This viscous and sweet-tasting liquid is solvable in water and is commonly known as an antifreeze mixture in this context.

This thesis contains pre-studies that are relevant for a planned X-ray beam time at DESY. The pressure dependence of glass transitions and the viscosity of glycerol will be investigated using X-ray scattering. To achieve this, gold nanoparticles are dispersed in glycerol, and the Brownian motion is observed via X-ray photon correlation spectroscopy (XPCVS).

The measurements will take place in a cryostat with the temperature controlled by a Si-diode. Since the sample is placed in the diamond anvil cell, several centimetres away from the diode, a temperature offset is expected. To determine this offset, an additional thermocouple is attached to the diamond cell. With this, I aim to determine the offset of the diode from the actual sample temperature. With a symmetric diamond anvil cell, I aim to transform liquid water to ice VI & ice VII and measure the corresponding Raman spectra. Furthermore, this thesis studies several glycerol-water solutions based on their Raman spectra.

2. Scientific background

2.1. Phase transitions in water and ice

Water is made up of two hydrogen atoms that bond to one oxygen atom. It is V-shaped at an angle of 105.97° (see figure 2.2a)). Because oxygen has a higher electronegativity than hydrogen, the shared electrons are pulled closer towards its nucleus and a dipole occurs. Because of this, water is considered a dipolar molecule. The two free electron pairs of the oxygen create hydrogen bonds with the lone pairs of the neighbouring water molecules.

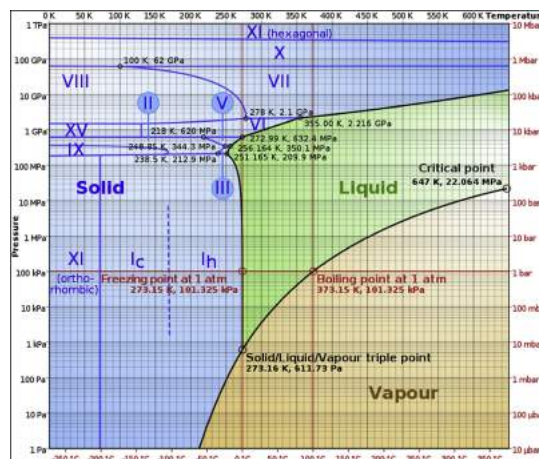


Figure 2.1.: Phase diagram of water [28], note the logarithmic scale on the ordinate.

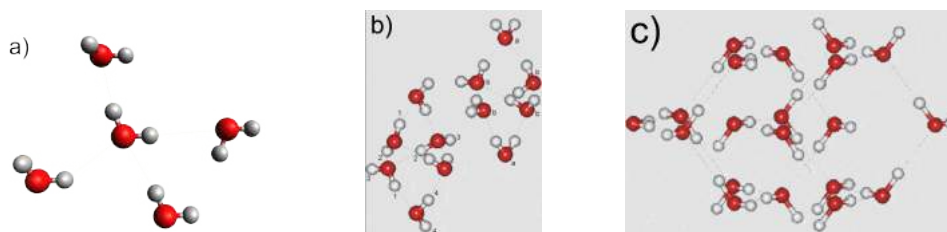


Figure 2.2.: structure of water (a) and crystal structure of ice vi (b) and ice vii (c); the oxygen in red and hydrogen in white. [8]

2. Scientific background

In figure 2.1 the complex phase diagram of water is shown. It has multiple triple points and one critical point (and a second liquid-liquid critical point) [8]. When applying pressure to water, at certain conditions, the hydrogen bonds start to undergo phase transitions to form different crystal structures. These structures depend on temperature and pressure. Through changes in pressure, water can solidify at different temperatures. The nineteen known ice phases can be divided into hydrogen-ordered and disordered ices [8]. The commonly referred-to ice is known as hexagonal ice (I_h). The phase boundaries between ices are mostly parallel to the temperature axis, which indicates density-dependent phase transitions. Transition boundaries parallel to the pressure axis indicate entropy-driven phase transformations. This is concluded in the Clausius-Clapeyron equation

$$\frac{dp}{dT} = \frac{\Delta S}{\Delta V} \quad . \quad (2.1)$$

It describes the slope of the boundaries between phase transitions, dp/dT , with ΔS , the difference in entropy, and ΔV , the volume difference of equal amounts of two phases. This volume difference then influences the density. [22]

In the pressure range of 0.6 GPa to 2.2 GPa, liquid water crystallises to **ice VI**. At this point, the tetrahedral networks form a crystal with two separate, non-interconnecting networks (fig. 2.2b)). Every water molecule has a hydrogen bond with four other water molecules. For two, they function as donors, and for two, they function as acceptors. The penetrating networks have no connecting hydrogen bonds but form packed octahedra.

In a range of 2.1 GPa to 62 GPa, ice VI transforms to **ice VII**. In the lower temperature range, ice VI first transforms into ice VIII and then into ice VII. Ice VII has a cubic crystal lattice with two interpenetrating cubic ice lattices (fig. 2.2 c)). Those hydrogen bonds pass through each other's water hexamers, but the lattices don't bond. [3,8]

2.2. Glycerol

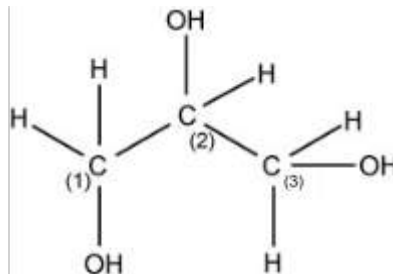


Figure 2.3.: Structural formula of glycerol and designation of the carbon atoms [19].

Glycerol, or propane-1,2,3-triol, consists of three carbon atoms with a hydroxyl group each. See fig. 2.3. Every oxygen atom in this constellation has two free electron pairs,

2. Scientific background

which can easily form hydrogen bonds. This makes the alcohol water-soluble. Due to its hygroscopicity, it also interacts with the water in the air. [11]

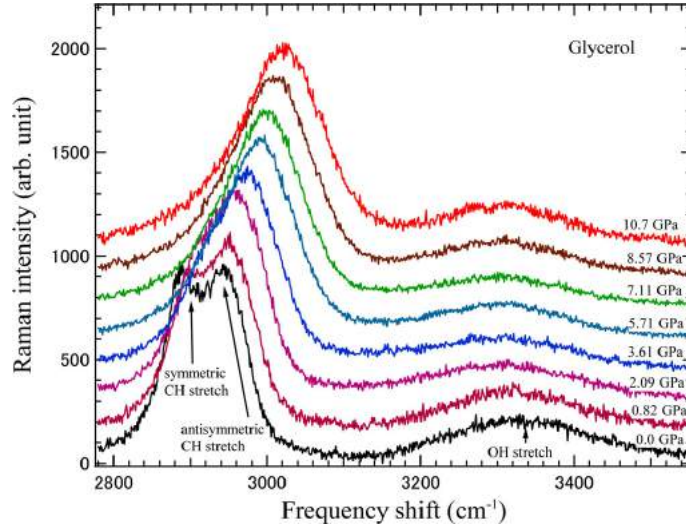


Figure 2.4.: Raman spectra of pure glycerol at high pressure [4]

With increasing pressure, the C-H stretching bands of glycerol shift to a more symmetric structure with the broadening of the bands. This can be seen in fig. 2.4, measured by Muhtar Ahart et al. [4]. Similar to water, this occurs in a range from ambient pressure to the glass transition pressure at about 5 GPa.

Some fluids, such as glycerol, can be cooled below their melting temperature T_m without crystallisation. Some start crystallisation after a critical temperature $\Delta T_{max} = T_m - T_{min}$, with T_{min} being the lowest temperature at which the fluid can be cooled without crystallisation. Others can be undercooled further to the glass transition temperature T_G where the melt behaves like a solid. This amorphous solid result of a cooling process without crystallisation is called glass. This is no first order phase transition. There is no abrupt change in a parameter during the glastransition, but by measuring the heat capacity during a cooling or heating process, T_G can be determined. Depending on the cooling or heating rate the glass transition occurs at different Temperatures, but this would exceed the scope of this thesis. A calimetric measurement of T_G of glycerol was done by C. A. Angell and is shown in figure 2.5 [5]. Such measurements conclude the melting temperature to be $T_m = 291$ K and the glass transition temperature to be at $T_G = 193$ K [22]. The peak of the heat capacity, or the glass transition temperature, is observed to be shifting to higher temperatures with increasing pressure, as illustrated in figure 2.6.

2. Scientific background

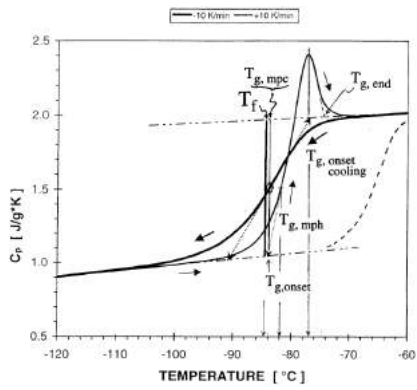


Figure 2.5.: Glass transition of glycerol according to differential scanning calorimetry [5]

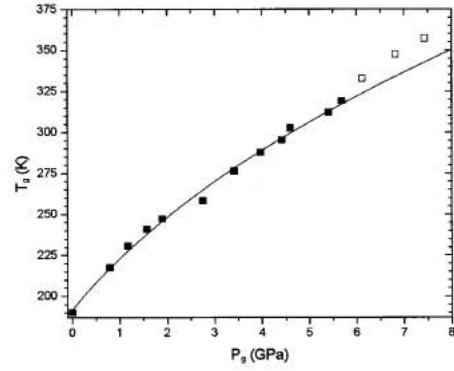


Figure 2.6.: Pressure dependence of T_G of glycerol obtained from dielectric relaxation measurements [20]

3. Experimental methods

3.1. The diamond anvil cell

3.1.1. Symmetric diamond anvil cell

The diamond anvil cell (DAC) is a high pressure cell consisting of two diamonds in a steel housing. The schematic in figure 3.1 shows the diamonds facing each other while sitting in their seats. They have Boehler-Almax design with a culet diameter of 0.80 mm [7]. With two left-handed and two right-handed screws, pressure can be applied to the sample. The latter is held in place by a gasket, in this case a steel plate of 250 μm thickness with a 500 μm hole (see Section 3.1.4).

For my measurements, two of those symmetric diamond anvil cells were used, one (DAC I) provided by the extreme conditions beamline at Petra III (DESY). The other one (DAC II) in the same design belongs to the research group. Figure 3.2 shows an image of DAC I. Through the hole in the top, the light shines on the diamond.

3.1.2. Mounting the diamond on the seat

Using this DAC design, the diamond and seat are fixed and cannot be tilted once glued to one another. That is why the alignment of the diamond in the seat has to be done diligently.

This was done using the Diacell Horizon and easyGlue [Almax easyLab]. After the diamond and seat are cleaned with acetone and ultrasound-bathing, they are inserted in the centre of the Diacell easyGlue. The laser from the Diacell Horizon shines from the bottom through the diamonds and is reflected by the culet and bottom of the diamond. The reflection is directed out of the laser box onto a wall. Additionally, the laser creates a laser spot on the same wall. By changing the position of the diamond in the cell, the positions of the laser spots are aligned on top of each other. If so, the diamond is aligned parallel to the orientation of the seat.

Due to the screws and springs in the Diacell easyGlue setup, the diamond can be held in this position and taken to a microscope, where it is fixed with epoxy glue. In this case, Lakeshore Stycast epoxy (ES-2-20) is used.

3.1.3. Aligning the diamonds in the cell

When the seats with the diamonds are placed in the steel frame of the DAC, they have to be aligned horizontally and on top of each other. To do this, four screws are used to secure each seat, enabling the cell's position to change. First, the diamonds are centred by eye, then the cell is closed and the diamonds are brought close together.

3. Experimental methods

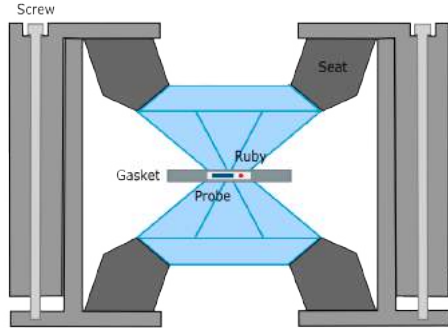


Figure 3.1.: Schematic of the DAC with its main components, not to scale, adapted from [2]



Figure 3.2.: Photo of DAC I

Now the culets are aligned by moving the seats around with the screws. Additionally, the facets have to be oriented towards each other. This is done carefully, without pressure, to reduce the chance of breaking the diamonds.

If the diamonds are brought together very closely, Newton rings appear. It can help to wet the culets. The number of Newton rings decreases with improved diamond alignment.

3.1.4. Preparing steel gaskets

Every time the diamonds are newly aligned, new gaskets have to be made. This is because the gaskets are usually pre-indented by the diamonds, so it could cause breaking if the pattern of the gasket and diamond do not match.

This experiment uses steel gaskets with an initial thickness of 0.250 mm and a diameter of 100 mm. It is placed centrally in the bottom part of the diamond anvil cell, and its position is marked. Afterwards, the cell is closed and pressure is applied. The two left- and right-handed screws help to apply the pressure evenly.

The indentation thins the steel and leaves a pattern in the gasket. With the help of the marking and this indentation, the gasket can slip into the same position every time. The thickness of the gasket should be reduced to around 0.05 mm.

Due to the breaking of one diamond, the process could not be continued within the timeframe of this thesis. Subsequently, a hole should have been drilled in the gasket. This can be done, for example, by using a conventional drill or microelectrical discharge machining (EDM) drilling.

3. Experimental methods

3.1.5. Preparing a sample

Ruby balls sized 3 μm to 50 μm in diameter are placed in the sample chamber inside the gasket. This is done with the help of the Leica M125C microscope. With a tungsten wire, a ruby ball is placed in the middle of the cleaned lower diamond. By positioning it in the centre, it can later help centre the gasket. This is done by placing the gasket in the cell according to its marking and moving it around until the ruby is seen through the hole of the gasket. Now, the cell can be closed carefully without applying pressure, so the gaskets slide in place. After opening the cell, the fluid of interest can be inserted and the cell closed again, ready for measurements.

3.2. Cryostat

In order to do temperature dependent measurements at cryogenic conditions, a cryostat was used. It consists of a vacuum chamber with four windows and can be opened and closed on the top. The lid has connections to the measuring instruments and a fume outlet. It holds the diode and a fitting for the diamond anvil cell. See figure 3.3a) & b). It is the model ST-400 ultra High Vacuum, manufactured by Lake Shore Cryotronics (Janis).

In this Bachelor thesis, I have implemented a new thermocouple sensor to the existing setup. To bring the thermocouple in the cell, the holder of the DAC had to be modified with a hole on the bottom. Like this, the thermocouple could be fed through the cover of the cryostat and the bottom of the fitting inside the cell to the gasket. See figure 3.3. It is glued with Lake Shore Stycast epoxy (ES-2-20) to the gasket with a thermal contact to the steel. The diode is connected to a Lake Shore Temperature Controller Model 335 with an integrated heater. The thermocouple is read out by the Keithley 2110 Series 5.5 Digit USB digital multimeter.

3.2.1. Principles and operation of thermocouples and diodes

A **thermocouple** consists of two electrical conductors made of different materials. They are connected in such a way that they only touch at two points. An intermediate voltmeter measures the voltage rising from the Seebeck effect when the two contact points have different temperatures. This voltage depends on the materials used and their respective Seebeck coefficients. By knowing these coefficients and the known temperature at one end of the conductor pair, a temperature sensor can be created. A thermocouple of type K consists of NiAl and NiCr and is well suited for low temperatures below -200°C . [10] [12]

As a semiconductor device, a **semiconductor diode** is based on the p-n junction of semiconductor crystals, which is temperature-dependent. Therefore, it can also be used as a temperature sensor. When a current is applied to a diode, the measured voltage drop can be used to infer the temperature. This is due to the bandgap that acceptors in the p-doped part of the semiconductor have to overcome, which is

3. Experimental methods

temperature-dependent. Through previous measurements, a calibration can be performed.

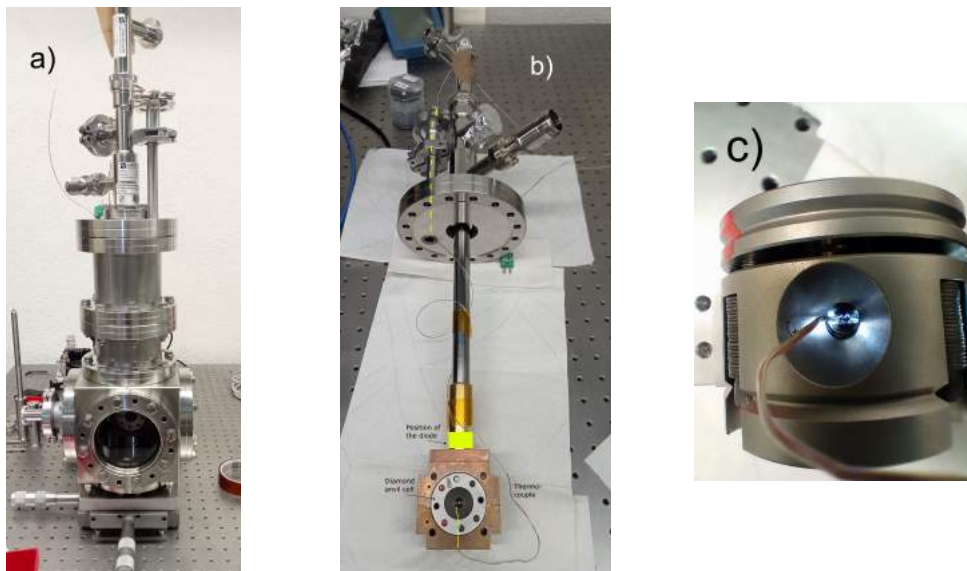


Figure 3.3.: (a) The closed cryostat (b) The arm with the diode and fitting with DAC and glued thermocouple; the yellow lines indicate the pathway of the thermocouple. (c) Closeup of the cell and the thermocouple glued to the gasket.

3.3. Raman spectroscopy

For these measurements, an existing setup from the research group of Prof. Dr. Weil at the Max-Planck Institute for Polymer Research in Mainz was used. The setup is used for measurements with a diamond anvil cell as well and includes a laser (LaserQuantum Tau532) with a wavelength of 532 nm. As shown schematically in figure 3.5, the laser is directed onto a sample in the diamond anvil cell using mirrors and lenses. The lenses focus the beam along its path. In the diamond anvil cell, the incoming light is reflected back until it reaches a dichroic mirror. This mirror reflects only a specific wavelength, in this case 532 nm, back to the laser to exterminate the Rayleigh scattering (section 3.3.2) .

The remaining light enters the dispersive spectrometer. The light is then reflected by a diverter mirror and shines, after passing another mirror, onto the grating. The latter is a diffractive element consisting of parallelly arranged 'lines'. Those reflect the light, creating different path lengths and therefore an interference pattern. The lines are called grooves, and the groove density ($\frac{g}{mm}$) states the number of grooves per millimetre. The higher the density, the higher the resolution. This has a limit for the incoming wavelength of $2/\text{groove} = \text{wavelength}$. The angle of the reflective

3. Experimental methods

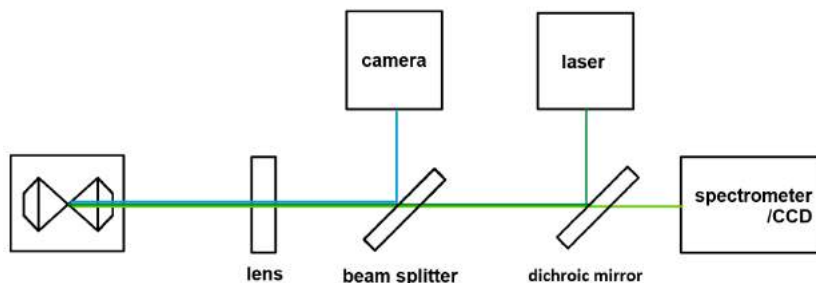


Figure 3.4.: Schematic of the beam path

grooves is called the blaze angle. With this, the efficiency of the grating at a specific wavelength can be increased. The reflected light is led to a Charge-Coupled Device (CCD) sensor. The CCD used here is from ThorLabs and cooled with liquid nitrogen to -180°C to reduce thermal noise.

To precisely target the DAC and the substances of interest with the laser, the position of the sample can be observed using an optical camera. The image is displayed on a computer through ThorCam. With the laser turned on, the position where the laser is visible in the image can be marked. With the laser turned off, the sample can be aligned using an XYZ-stage so that the laser irradiates the desired spot. As the sample is moved along the direction of the laser beam, it shifts in focus, allowing the measurement of different points.

The spectrometer with a CCD sensor and the laser can be controlled through the connected computer. Using the RemoteApp Laser Control from Laser Quantum, the laser power can be continuously adjusted. With the Lightfield software from Teledyne Princeton Instruments, parameters such as exposure time, number of acquisitions, acquisition range, and the Grating can be set.

The setup provides two gratings. The one mainly used in the measurements has a Density of $300 \frac{g}{mm}$ and is blazed at 500 nm. The second one with higher resolution due to the higher Density of $1800 \frac{g}{mm}$ is blazed at 500 nm. The entrance slit to the spectrometer is 300 μm wide. Furthermore, the setup has a filter to decrease the power of the laser beam. It was not permanently placed in the beam path.

3.3.1. Ruby fluorescence

When light interacts with a molecule, it excites electrons, depending on the wavelength. The electrons are only elevated to the next excited electronic state if the wavelength provides the characteristic energy. Suppose an electron, excited from its vibrational ground state to the first excited state. Then it deexcites and returns to the vibrational ground state. During deexcitation, it emits light with an energy equal to the gap of the excited and ground states. This energy determines the emitted wavelength of the photon. This is called fluorescence and is illustrated in fig. 3.5 on the

3. Experimental methods

outer left.

In ruby crystals, fluorescence appears due to Cr^{3+} ions. The ruby in this setup consists of corundum (Al_2O_3) with chromium atoms replacing some aluminium atoms. The characteristic wavelength depends on the temperature, pressure, and Cr concentration. The wavelength shift is the sum of the shifts of each factor. The effect of the Cr concentration is neglected for the following measurements, because I used the same rubies for all measurements. All were produced by BETSA. For a constant temperature, the shift depends on the pressure applied to the ruby. With this, the pressure on the ruby can be determined by the fluorescence signal. [9, 13, 23].

3.3.2. Raman scattering

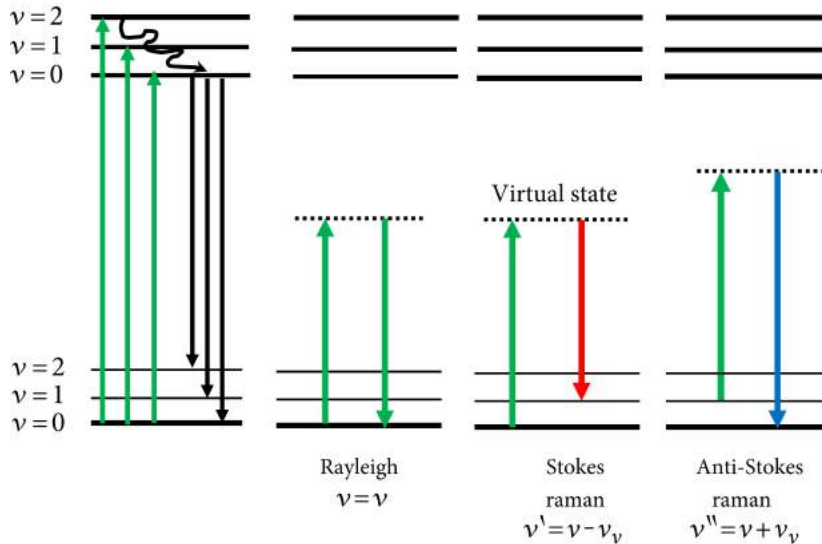


Figure 3.5.: Schematic figure of energy levels of a molecule with the vibrational states $\nu = 0, 1, 2$ within the electronic states. ν' and ν'' represent the outgoing wavelength adapted from [17].

If the energy of the light does not coincide with the energy of the first excited state, then the molecule can be elevated into a so-called virtual state.

When the molecule falls back to the vibrational ground state, it is called **Rayleigh scattering**, fig. 3.5 inner left. In this process, the same wavelength is emitted, which excites the molecule. In Raman spectroscopy, this scattering is not desirable as it prevents making accurate statements about vibrational energy levels.

If the particle does not fall back to the vibrational ground but excited state, it emits light shorter than the excitation wavelength. (Fig. 3.5 inner right.) This **Stokes scattering** gives information about the vibrational energy level. Since the incoming wavelength is known and the outgoing wavelength can be measured, the energy differences can be determined.

3. Experimental methods

The **Anti-Stokes scattering** occurs if the particle is excited from its virtual excited state and falls, after the excitation in the virtual state, back to its ground state. (Fig. 3.5 outer right.) Similar to Stokes scattering, this gives insights into the vibrational energy level.

Due to the Boltzmann distribution, there are more electrons in the ground state than in the vibrational states. As the excitation levels increase, the likelihood of particles decreases. That's why it is more probable and efficient to measure Stokes scattering than anti-Stokes scattering. When selecting the laser for the experiment, it's therefore essential to ensure that its wavelength is insufficient to excite the particles to their first electronic state. The laser should only elevate the particles to a virtual state. [21]

3.4. Preparation of glycerol-water mixtures

The glycerol used for the experiments has a concentration of >99.5% [Sigma-Aldrich]. The solutions were made in a nitrogen atmosphere due to the hygroscopic nature of glycerol. The water used is called MilliQ Water. This is high-purity water, cleaned with UV light and ultrafiltration by the Sartorius Arium 611 VF Water Purifier. When water is mentioned in the following, unless otherwise specified, it refers to water purified in this manner.

For the experiment, mixtures with different mole percentages and one mixture with mass percentages were prepared.

The mixtures in **mole percentages** were prepared by filling water into a vial using a syringe. Subsequently, it was purged with gaseous nitrogen to displace the air. Then, glycerol was injected into the container with a syringe, followed by closing the lid and sealing it with ParaFilm.

The fraction of glycerol in the glycerol-water solution can be determined by

$$\chi = \frac{\frac{\rho_G}{M_G} V_G}{\frac{\rho_G}{M_G} V_G + \frac{\rho_H}{M_H} V_H} \quad (3.1)$$

With ρ_G being the density of glycerol, M_G the molar mass of glycerol, V_G the volume of glycerol and the corresponding values of water indicated with H .

So, the amount of glycerol required to achieve a specified percentage of glycerol in water can be determined through:

$$V_G = \frac{\chi}{1 - \chi} \cdot \frac{M_G \rho_H}{M_H \rho_G} \cdot V_H \quad (3.2)$$

The molar mass and density of glycerol were given by the company [Sigma-Aldrich, product G7893-21]. The information from Water is drawn from [1, 24]. Therefore the values are assumed error-free.

$$M_G = 92.09 \frac{g}{mol} \quad \rho_G = 1.25 \frac{g}{cm^3} \quad (3.3)$$

$$M_H = 18.0153 \frac{g}{mol} \quad \rho_G = 0.9982 \frac{g}{cm^3} \quad (3.4)$$

3. Experimental methods

χ [%]	V_G [ml]	ΔV_G [ml]	V_H [ml]	ΔV_H [ml]	$\Delta\chi$ [%]
2	10	0.5	0.833	0.1	0.2549
5	10	0.5	2.15	0.2	0.50197
7	10	0.5	3.07	0.2	0.5342
10	10	0.5	4.54	0.2	0.6002
15	10	0.5	7.20	0.5	1.0907
20	5	0.2	5.10	0.2	0.896
35	5	0.2	10.99	0.5	1.3782
50	3	0.2	12.25	0.5	1.95442

Table 3.1.: Composition of glycerol and water of the different mixtures.

Since the volumes of added water and glycerol are subject to errors caused by air in the syringe, residues on the syringe, and inaccuracies during the filling process, an error in the size of the calibration scale is assumed here. This error varies depending on the type of syringe used. 10 ml, 5 ml, and 1 ml syringes were available. The errors on the percentage values were calculated with equ. 3.5 and can be found in the following table. Additionally, the prepared solutions with the corresponding millilitre values are listed.

$$\Delta\chi = \sqrt{\left(\frac{\frac{\rho_G}{M_G} \frac{\rho_H}{M_H}}{\left(\frac{\rho_G}{M_G} V_G + \frac{\rho_H}{M_H} V_H\right)^2} V_H \cdot \Delta V_G\right)^2 + \left(\frac{\frac{\rho_G}{M_G} \frac{\rho_H}{M_H}}{\left(\frac{\rho_G}{M_G} V_G + \frac{\rho_H}{M_H} V_H\right)^2} V_G \cdot \Delta V_H\right)^2} \quad (3.5)$$

For the mixture in **mass percentages** the goal was to make a solution of 50% glycerol and 50% water. To do this, the same amount of water and glycerol was weight in a vial. After the water was inside the vial, it was filled with gaseous nitrogen and sealed with ParaFilm. Then the glycerol was injected with a syringe to minimise the contact of the glycerol with the air in the room.

This solution's error can be identified by

$$\begin{aligned} \Delta\chi &= \sqrt{\left(\left[\frac{d}{d m_G} \frac{\frac{m_G}{M_G}}{\frac{m_G}{M_G} + \frac{m_H}{M_H}}\right] \cdot \Delta m_G\right)^2 + \left(\left[\frac{d}{d m_H} \frac{\frac{m_G}{M_G}}{\frac{m_G}{M_G} + \frac{m_H}{M_H}}\right] \cdot \Delta m_H\right)^2} \\ &= \sqrt{\left(\frac{M_G M_H m_h}{(M_G m_H + M_H m_G)^2} \Delta m_G\right)^2 + \left(\frac{M_G M_H m_g}{(M_G m_H + M_H m_G)^2} \Delta m_H\right)^2} . \end{aligned} \quad (3.6)$$

With $m_H = (7.0000 \pm 0.0001)ml$ and $m_G = (7.0009 \pm 0.0001)ml$ one receives $\Delta\chi = 0.000\ 002\ 765$.

4. Results of the temperature calibration

4.1. Cooling the cryostat with nitrogen

Before starting the measurement, the cryostat is connected to a tank of liquid nitrogen. The tank is pressurised to 0.3 bar by using gaseous nitrogen, allowing the cryostat to be cooled through a transfer line. The diode is located at the bottom of the cold head. The excess gas is extracted directly from the cryostat into the flue of the laboratory. The valve on the transfer line is opened by two full turns to release nitrogen in the cryostat. The chamber is evacuated to create a vacuum of 6.3×10^{-4} mbar to 3.0×10^{-4} mbar.

The following measurement was taken four times. The first three times with DAC I, filled with water. The fourth setting contained the DAC II without a water probe and a gasket of 130 mm.

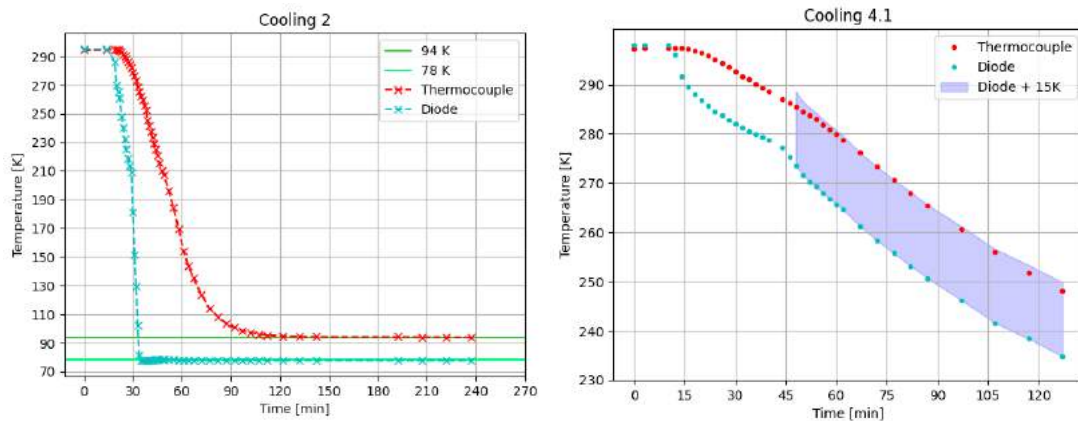


Figure 4.1.: Left: Complete cooling of the cryostat in the first turn.
Right: Cooling in the second setup; plotted in the range of 300 K to 235 K
The discontinuities in the temperature drop can be ascribed to the varying nitrogen supply

When the valve to the cryostat is opened, the interior starts to cool down to the boiling point of nitrogen, which is 77.2 K. In the left graphic of figure 4.1 this process is displayed. Figure 4.1, right, shows another measurement in the temperature range down

4. Results of the temperature calibration

to 235 K. Here, the cooling rate was slow. When the nitrogen enters the cryostat, it passes the diode first. Here, the copper fitting of the diamond anvil cell and the cell itself had to cool down before the sample could adjust their temperatures. This causes the temperature differences between the diode and the thermocouple, which is attached to the gasket, to be as close as possible to the sample itself. Even though the temperature decrease in measurement 4 happened slower, the temperature differences between the diode and the thermocouple stayed at about 15 K. This is due to the cooling of the copper fitting, which needs to be cooled first. This is also observed at the equilibrated temperatures. The diode equilibrated after 22 min at (77.7 ± 0.1) K, and the thermocouple after 108 min at (94.0 ± 0.5) K. There is a temperature decrease of 0.2 K seen over 2 h, indicating further cooling of the gasket. The duration differs in all four measurements, but the thermocouple always took a minimum of 40 min longer to equilibrate.

The temperature difference of (16.3 ± 0.6) K is higher than observed in the cooling process of measurement 4. This discrepancy can be caused by measurement errors or the slightly different positions of the thermocouple in the last measurement. Furthermore, during the cooling process, the thermocouple and the fitting continue cooling, so it is more likely to have a smaller temperature difference than in the equilibrated state.

4.2. Heating the cryostat with the diode

For heating, the nitrogen was still connected and could be controlled by the diode and in-built heater. In the range up to 110 K, the heater of the instruments was not working as supposed. It seemed to be heating up, but the temperature did not change. Only when a setpoint of 110 K was indicated did the temperature sensor show a rising temperature.

In the measurement displayed in figure 4.2 the data until minute 49 is neglected since it shows the process of finding a temperature at which the heater starts working. This and the previous heating processes are shown in the appendix. There, the heating setpoint was increased 15 minutes after the diode reached the previous setpoint temperature. The thermocouple does not fully equilibrate within this timeframe, and the data is therefore neglected.

4. Results of the temperature calibration

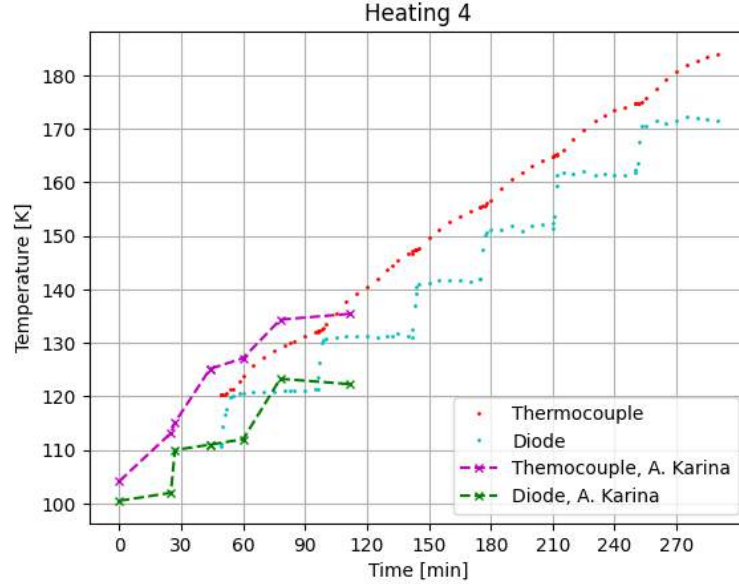


Figure 4.2.: Heating process of DAC II and a previous measurement of Aigerim Karina. The data can be found in the appendix, table A.1

In measurement 4, the temperature trend at a setpoint was measured until the temperature of the thermocouple did not change more than 1.5 K in 10 minutes. As half an hour is the time frame of a measurement during a beam time, this covers the region of interest. Table 4.1 presents the temperature of the diode and thermocouple when the setpoint was induced, when the diode hit the setpoint, and when the thermocouple did not change more than 1.5 K per 10 min. The diode reached the setpoint in not more than 1 minute. It fluctuates, especially in the higher temperature regions, about 2.5 K, but the heater keeps the diode around the desired temperature. The Thermopoule reacts in under a minute to the diode. This corresponds to the cooling process, but now the copper block has to heat up and then heat up the DAC and gasket. The thermocouple takes between 31 min and 44 min to equilibrate after the diode reaches the setpoint. The differences in temperatures at these points are between 10.73 K and 15.87 K. It should be noted that the higher temperature differences do not necessarily correspond to the longer equilibration time. The mean of the temperature differences is (12.87 ± 0.22) K. This is smaller than the offset observed in the cooling process. But there, the measurement took longer. Here, the temperature was still slightly rising. Therefore, the true equilibrated temperature can be higher than 12.87 K. Additionally, only one dataset was taken at a time, and the fluctuation of the diode took some time for the instrument to compensate. This can be seen in the table between the last dataset before and after the new setpoint.

Besides the measured data, figure 4.2 shows a dataset from a previous measurement. This was done by a member of the research group. There, the setup differs slightly, with the thermocouple glued from the outside to the diamond of the DAC. The ob-

4. Results of the temperature calibration

served equilibration time is in accordance with what is observed in this thesis. The temperature offset is, with an average of 13.15 K, higher than observed in this measurement. This was expected the other way around, since the nitrogen first cools the diamond and then the gasket. But given the error range, the mentioned fluctuations in the temperature of the diode, and some datasets having an offset of over 15 K, the data provides results compatible with the previous measurement.

Setpoint [K]	Time [min]	temp. Diode [K]	temp. Thermocouple [K]
120	49	111.17	120.44
	55	120.20	121.39
	95	121.24	131.97
130	96	121.30	132.14
	98	130.01	132.83
	142	131.12	146.99
140	142	132.61	147.15
	144	140.54	147.55
	175	141.93	155.27
150	175	142.08	155.35
	177	150.21	155.69
	210	152.49	164.90
160	210	151.33	164.94
	212	159.31	165.10
	250	162.37	174.75
170	250	161.85	174.77
	253	170.56	175.05
	290	171.52	183.98

Table 4.1.: For the sake of clarity, the uncertainties were not added to the measured values. They are assumed as $\Delta t = \pm 1 \text{ min}$, $\Delta T_D = \pm 0.50 \text{ K}$, $\Delta T_{TC} = \pm 0.05 \text{ K}$

It should be noted that the diode and thermocouple were not read out by the same instrument. Since no digital readout could be accomplished, the data pair was recorded by taking a photo of the displays of the instruments. This way, the data were taken at the same time. Additionally, there is an error due to the length of the thermocouple. Over the $(201.5 \pm 0.7) \text{ cm}$, the loss over the conductor affects uncertainty as well as physical deformation. Furthermore, the connection of the thermocouple to the instrument can cause a systematic error in the setup.

5. Results of the Raman spectroscopy

In this chapter, Raman measurements of water at elevated pressure and glycerol at ambient pressure are summarised. For this thesis, I had to make a new aluminium adapter plate in order to mount our DAC to the Raman setup. This plate is indented, so the cell can always be placed in the same position. This way, the orientation of the laser can be restored more easily.

For the analysis, Gaussian curves are fitted to the acquired data. This was done with an orthogonal distance (ODR) regression in Python. In the appendix, the raw data and corresponding fits are shown. There, the reduced Chi square can also be found. Error of the intensity is assumed to be 0.01, as it is the precision of the instrument; the error of the wavelength is assumed to be 0.00001 nm.

5.1. Phase transitions of water at room temperature

5.1.1. Pressure determination

For the temperature assumed to be constant, the wavelengths of the ruby peaks (called R1 (higher wavelength) and R2 (lower wavelength)) are directly correlated to the pressure P . This leads to a commonly used approach to determining the pressure inside the diamond anvil cell. Equation 5.1 finds the pressure difference between the measured wavelength λ and λ_0 the reference wavelength λ_0 . A and B are calibration constants [15].

$$P(\text{GPa}) = \frac{A}{B} \left[\left(\frac{\lambda}{\lambda_0} \right)^B - 1 \right] \quad (5.1)$$

I used the *Flourescence pressure calculation and thermocouple tools* website [13] which calculates pressure using the reference database [23]. The temperature correction is based on Datchi et al., 2007 [9].

When applying pressure, the R1 and R2 of the ruby shift to higher wavelengths. In figure 5.2b) such a shift is shown as exemplary. Fit 1 to Fit 11 are the measured spectra during the recording of the water-ice transformation at room temperature. According to literature [16, 23] the R1 peak at ambient pressure lies near 694.25 nm. To calculate a reference specific for this setup, a total of seven measurements on different ruby balls were taken. Those are shown in figure 5.1. Contrary to expectations, the peak position of the R1 line varies up to 0.703 nm around a mean of 693.911 nm. This broad range can be caused by off-centre laser positions, different foci, and different ruby balls. Even though the calculated reference line lies below the literature, it is still higher than expected. The measured spectra during the water-measurements

5. Results of the Raman spectroscopy

show peaks at 693 nm (tab. 5.2). This leads to negative pressures, that are not physically meaningful.

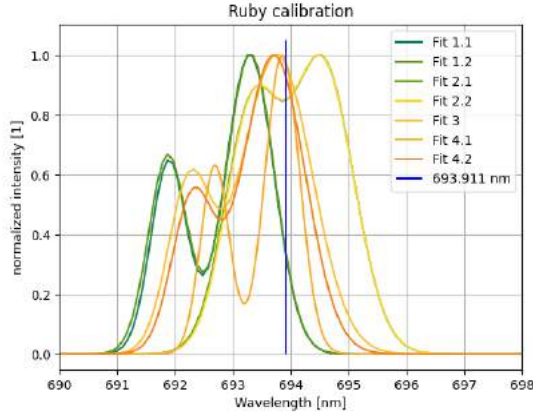


Figure 5.1.: Normalized Raman spectra of different rubies at ambient pressure. The blue line marks the mean of the R1 peaks at (693.911 ± 0.014) nm.

5.1.2. Water phase transition

This measurement was taken with the diamond anvil cell I; filled with water and a ruby ball. From the beginning, the data were gathered in the centre of the sample chamber, see figure 5.2. With increasing pressure, I started measuring at two more positions at the border of the gasket, since it is more likely to see the phase transition here first. For the measurements of water, the filter was taken out of the beam path and the laser power set to 3.2 mW. The laser power always fluctuated by about 0.1 mW. For each pressure step or partial measurement, a dataset of five frames at 50 seconds each was recorded. For the accumulation of ruby spectra, the filter was placed in the path of the laser, and the initial laser power was set to 5.0 mW. The acquired datasets consist of five frames at 2 seconds each. To observe the phase transition, the Raman spectrum of water and the spectrum of a ruby were acquired. After measuring the water and ruby at one pressure, the DAC was taken out of the setup and the pressure increased.

In figure 5.3, the spectra of the ruby are collected. Contrary to expectations, the measured ruby signal does not increase continuously. The first peak of the R1 line is shifted to a higher wavenumber than the seventh. Similarly, the third is higher than the sixth. This can be caused by different positions of the laser when measuring the spectrum. The laser's position could not be restored exactly after taking the DAC out, despite being marked and photographed in the previous measurement. The first data were taken with the laser centred on the ruby, and the second and following data were measured slightly off-centre to have consistent data. But nevertheless this causes uncertainty in the pressure because the reference is not the same as for the centred

5. Results of the Raman spectroscopy

beam position.

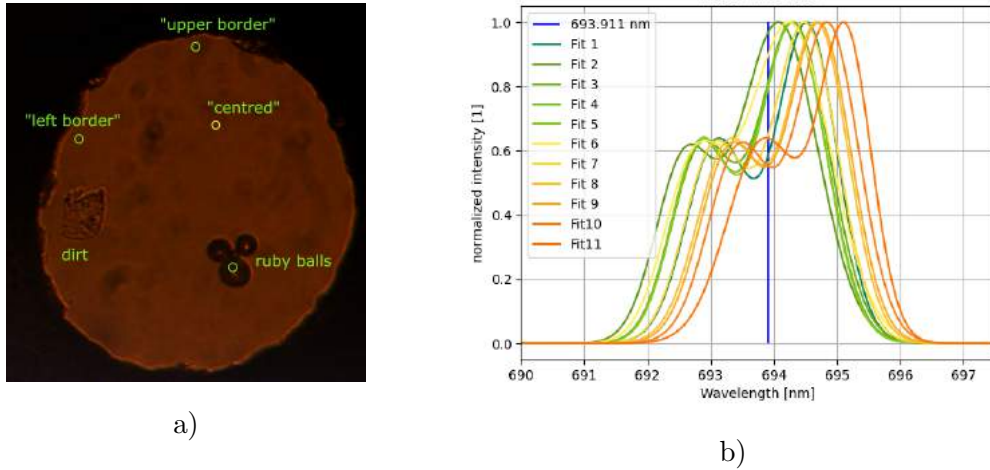


Figure 5.2.: a) Laser positions during the measurements. The green markings are inserted afterwards. The position of the 'centred' position is of the real centre to reduce the remaining signal of the rubies.
 b) Normalised Raman spectra of the ruby for each pressure step during measurement 5. The blue line marks the calculated reference for ambient pressure

Figures 5.3a)-c) show the Raman spectra of water, with the OH stretch band centred around 3200 $1/\text{cm}$ and 3400 $1/\text{cm}$. Displayed is the mean of the five acquired frames of each dataset. Up to measurement 9, at a pressure of 2.22 GPa, no phase transition is observed. But the clarity of the peaks of the OH stretches decreases. This is a sign of the upcoming phase transition. At 2.58 GPa, a transformation of water to ice VI shows up at all three observed positions. The spectra display the peak with the highest intensity around 3200 $1/\text{cm}$ with two lower peaks in a higher wavenumber. The strongest signal belongs to the coupled, in-phase, OH-stretch. But since the literature shows more distinct peaks for a full transformation, it can be assumed that the transition did not complete [14, 25]. As introduced in Section 2.1, the phase transition of liquid water to ice VI is determined in a range up to 2.2 GPa. The later transformation is mostly because of the pressure determination. This also applies to the transformation to ice VII.

5. Results of the Raman spectroscopy

Dataset	R1 [nm]	$\Delta R1[nm]$	R2 [nm]	$\Delta R2[nm]$	P [GPa]	$\Delta P[GPa]$
1	694.522	0.005	693.057	0.008	1.65	0.05
2	694.067	0.005	692.538	0.007	0.42	0.04
3	694.301	0.005	692.801	0.007	1.05	0.05
4	694.282	0.005	692.781	0.006	1.00	0.05
5	694.293	0.005	692.799	0.007	1.03	0.05
6	694.231	0.005	692.704	0.007	0.86	0.05
7	694.490	0.005	692.988	0.007	1.57	0.05
8	694.696	0.005	693.197	0.007	2.13	0.04
9	694.729	0.005	693.216	0.007	2.22	0.04
10	694.862	0.006	693.348	0.008	2.58	0.05
11	695.182	0.008	693.693	0.011	3.46	0.05

Table 5.1.: The pressure is calculated with [13] in reference to 683.911 nm at the R1 peak. The error to the pressure is assumed with the uncertainty of the wavelength and reference peak.

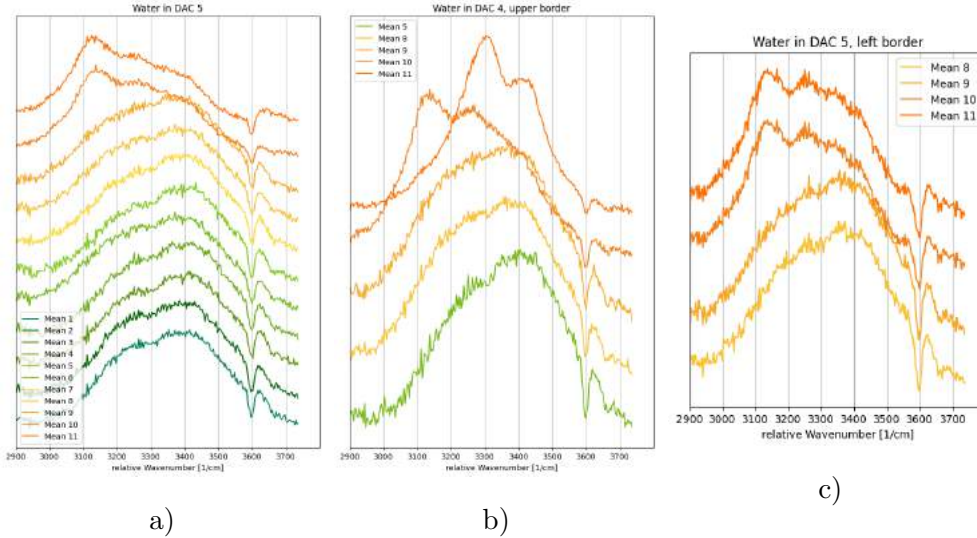


Figure 5.3.: Raman spectra of water at the centre (a) , upper border (b) and left border (c) of the sample chamber

While the ice in the centre of the cell stays in this form, the ice on the borders transforms at a pressure of 3.43 GPa to ice VII. This pressure is higher than the predicted 2.2 GPa at room temperature. the transformation can be seen by the intense peak around 3300 1/cm. This and the smaller peak at 3400 1/cm correspond to the O-H stretching modes. In the spectrum of the left border, a superposition of ice VI and ice VII can be seen. The small bump in dataset 11 at 3100 1/cm is a sign of remaining ice VI in ice VII.

5. Results of the Raman spectroscopy

5.1.3. Water and air bubble in DAC

This measurement was also taken with the diamond anvil cell I; filled with water and a ruby ball. In addition, there was a bubble of air captured in the sample chamber during the closing of the cell. The data was gathered in the centre of the sample chamber, see figure 5.4. For the measurements of the water, the filter was taken out of the beam path and the laser power set to 13.1 mW. The laser power fluctuated by about 0.1 mW. For each pressure step or partial measurement, a dataset of five frames at 20 seconds each was recorded. For the ruby spectra, the filter was placed in the path of the laser and the initial laser power set to 4.7 mW until measurement 6. From measurement 7 on, it was set to 6.0 mW. The acquired datasets consist of five frames at 1 second each.

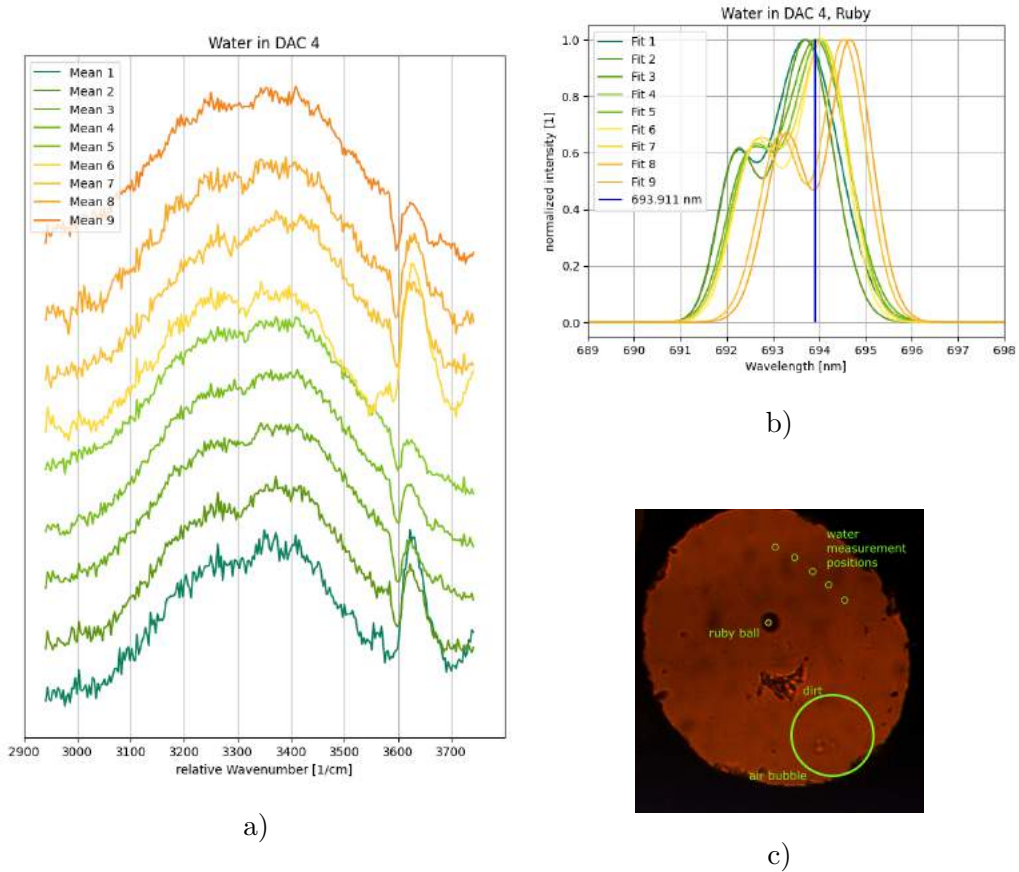


Figure 5.4.: a) Raman spectra of water in DAC I with elevating pressure.
b) Raman spectra of rubies at increasing pressure. The blue line marks the reference lines for ambient pressure.
c) Laser positions in the cell. The green markings are inserted afterwards. The big circle marks the initial position and size of the air bubble.

5. Results of the Raman spectroscopy

Dataset	R1 [nm]	$\Delta R1[nm]$	R2 [nm]	$\Delta R2[nm]$	P [GPa]	$\Delta P[GPa]$
1	693.697	0.005	692.137	0.007	-0.58	0.05
2	693.708	0.005	692.188	0.007	-0.55	0.05
3	693.912	0.006	692.369	0.008	0.00	0.05
4	693.989	0.006	692.472	0.008	0.21	0.05
5	693.972	0.005	692.441	0.008	0.16	0.05
6	694.064	0.004	692.591	0.007	0.41	0.04
7	694.076	0.004	692.591	0.009	0.45	0.05
8	694.552	0.006	693.092	0.005	1.74	0.05
9	694.685	0.005	693.236	0.007	2.10	0.04

Table 5.2.: The pressure is calculated with [13] in reference to 683.911 nm at the R1 peak. The error to the pressure is assumed with the uncertainty of the wavelength and reference peak

The reference wavelength for the pressure calibration is assumed to be 693.911 nm, which is not physically meaningful, since the first two datasets would lead to negative pressure. As mentioned this is most likely caused by different laser positions.

The enclosed bubble decreased with increasing pressure but was not squeezed out until measurement 8. Nevertheless, the data, shown in figure 5.4a), seemed to start transforming to ice VI as the clear peak around 3380 1/cm decreases by measurement 6. But the following data show no further transformation. Up to a pressure of 2.10 GPa, no distinct peak of ice VI shows up in the spectrum. Since the data were acquired at different positions (see fig. 5.4c)), this could lead to the decreasing of the OH stretch only being visible in one of the datasets. The fluctuations in the spectra can be caused by different measurement positions (see fig. 5.4c)) or by unwittingly changing foci.

At 3610 1/cm the spectra show a peak, which forms with increasing pressure in the broad peak of the OH stretches. This can be assigned to the stretching vibration mode of a free H_2O molecule [8, 26]. Due to the air bubble and the compressibility of the air, the pressure on the water is smaller. Therefore, the pressure applied to the cell has to be higher than in a cell with only water to see a transformation. I decided to interrupt the measurement and start a new one without a bubble (Measurement 5, Section 5.1.2).

5.2. Raman spectrum of pure glycerol

To compare the following measurements of different glycerol-water solutions, I first measured a spectrum of pure glycerol. To do so, I positioned a microscope slide instead of the DAC in the setup. On this, a rubber ring with an inner diameter of 0.9 cm is placed. This holds the glycerol sample. The laser power during this measurement is set to (5.1 ± 0.1) mW without the filter. The dataset consists of five frames of 60 seconds each.

5. Results of the Raman spectroscopy

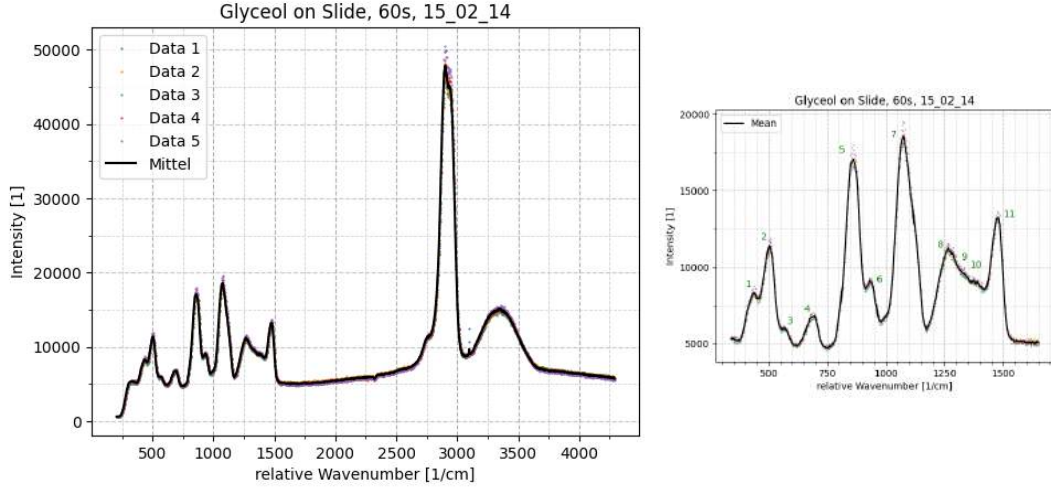


Figure 5.5.: Raman spectra of pure glycerol. The right shows a cutout of the lower wavelength region.

In the following, the measured peaks are assigned to Mendelovici et al. [18].

Glycerol has, similar to water, a peak between 3200 1/cm and 3500 1/cm. This corresponds to the antisymmetric and symmetric OH stretches. Between 2750 1/cm and 3000 1/cm the spectrum shows a sharp double peak. Those belong to the symmetric (lower wavenumber) and antisymmetric (higher wavenumber) CH stretches from the CH₂.

On the lower end of the spectrum, in the range of 350 1/cm to 1550 1/cm, multiple signals are measured. To assign those, Gaussian fits of the peaks 1-8 and 11 were created and compared with the data of Mendelovici [19]. The points 9 and 10 were assigned without mathematical analysis. The result is presented in table 5.3.

5. Results of the Raman spectroscopy

Peak	Wavenumber [1/cm]	Assignment
1	438	CCO rock
2	499	CCO rock
3	566	CCC bend
4	684	CCO bend
5	858	CC stretch
6	933	CH-2 rock
7	1075	CH-2 twist
8	1270	CH-2 twist
9		CH-2 twist
10		COH bend
11	1471	CH-2 bend

Table 5.3.: The measured peak wavenumbers and corresponding vibrational modes, assigned with [19].

[18] Additionally, there should be a signal from the CO stretch of the C-2 at around 1115 1/cm. A curve in peak 7 could be a hint to that, but it can also be peak broadening.

5.3. Raman spectra of glycerol-water mixtures

As described in chapter 3.6 several glycerol-water mixtures have been prepared. Due to the breakage of the diamonds, only measurements at ambient pressure could be done within the timeframe of this thesis. The mixtures are filled in a ring on a microscopic slide similar to the pure glycerol and covered with another glass slide. The laser power was set to (5.0 ± 0.1) mW and the data were acquired in five frames with 60 seconds for every solution.

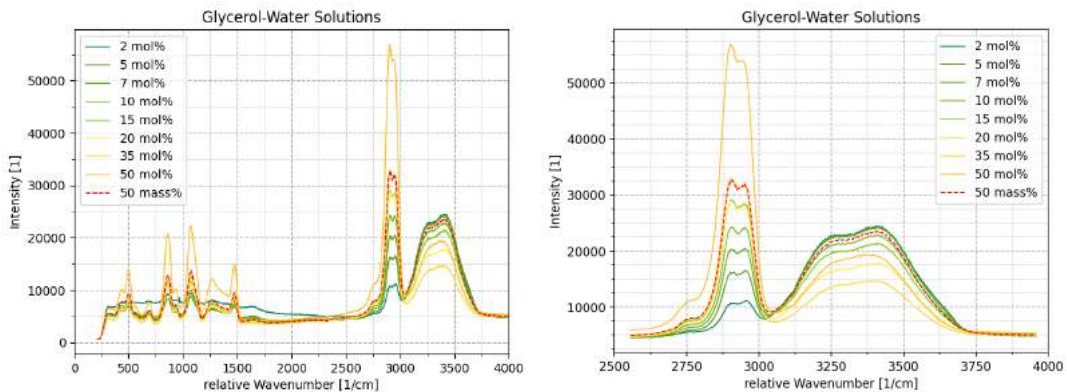


Figure 5.6.: Raman spectrum of glycerol-water solutions. The right shows a cutout of the high wavenumber region.

5. Results of the Raman spectroscopy

Figure 5.6 shows the spectra of the glycerol-water mixtures. The analysis of the measurement will focus on the high wavenumber range (2750 1/cm to 3750 1/cm) since the spectra in the low wavenumber range are not as distinguishable and the water signal can be observed better in the high wavenumber region. The data, shown in the appendix (fig. A.8), show an expanding intensity-signal in the low wavenumber region at multiple concentrations. This could be caused by increasing laser power during the measurement. The signals displayed in figure 5.6 display the mean of the five data frames.

In the range of 3000 1/cm to 3800 1/cm, the double peak of water superimposed the broad peak of the glycerol. Therefore, the sharp double peak of glycerol around 2900 1/cm can give information about the concentration of glycerol. The data for the 2 %, 5 %, 7 % and 10 % are as expected. With rising glycerol concentrations, the glycerol peak rises. The water peak is decreasing, which can be explained by the decreasing water fraction. Since the signal of the glycerol in this range is increasing too, this decreasing signal is composed of a shrinking water fraction and a rising glycerol fraction. This shows that the water has a greater impact on the peak than the glycerol at this concentrations.

While separated in the water peaks, the intensity of the 15 % and 20 % data overlaps in the glycerol peak. Also, the measurement of 35% glycerol intensity is lower than expected. Similar, the solution of 50 mass percentages is expected to have an intensity similar to that 15 mol% because it corresponds to 16 mole percents. But the signal of the OH-stretches of glycerol indicates a much higher concentration, such as 35 mol%. The signal of the stretching modes of water, however, indicates a concentration of seven to ten mol percentages. This could be caused by different settings, such as the focus or laser intensity. As described, the samples were measured on a microscopic slide, which was taken out of the setup, cleaned, and refilled after every measurement. Even though the focus was not changed during the measurements, removing and inserting can cause different foci. Another explanation could be the inhomogeneity of the solution. Water is known for accumulating in glycerol solutions. It starts to form clusters, especially at low temperatures (77 K) and increasing pressure [6, 27]. Since the experiment is done at room temperature and ambient pressure, this process is considered unlikely. The inhomogeneity could rather stem from incompletely dissolved glycerol. After setting the solutions aside for a day, the glycerol separated from the water. I could have taken a sample of a different solution as supposed, due to not properly mixing.

With the mole fraction increased to 50 percent, the signal of the glycerol and water peaks rises. Since the water peak is expected to sink with decreasing water fraction, this could be caused by an external factor, such as laser power, or the glycerol signal starting to superimpose the water signal. In the pure glycerol spectrum, the ratio of the CH stretch peak to the OH stretch peak is about 1:5. Transferred to this spectrum, the intensity of the OH stretch peak meets expectations.

6. Summary and outlook

In this thesis, glycerol and water in a diamond anvil cell were studied. This was done using Raman spectroscopy. Additionally, the temperature offset between a sample and a diode inside a cryostat was investigated. For both measurements, mechanical developments needed to be implemented.

The calibration of the sample temperature was done with a thermocouple brought next to the sample. The offset measured during the cooling process is (16.3 ± 0.6) K and above the calculated mean of the equilibrated temperatures of the heating process (12.87 ± 0.22) K. This was expected since the equilibration time of 30 minutes seemed not long enough for the thermocouple to equilibrate. The setup could be improved, and the equilibration time reduced, by adding thermal paste to the gap between the DAC and its holder to increase the thermal conductivity. Secondary, the Thermocouple could be shorter, and the instruments could read out digitally to decrease the uncertainties.

Raman spectra of water and glycerol solutions have been measured in order to test the current setup. With the diamond anvil cell, I successfully transformed water into ice VI and ice VII. To determine the pressure, I measured ruby balls at ambient pressure and derived a reference R1 peak of (693.911 ± 0.014) nm. This is higher than expected since it is bigger than some of the measurement points, but lower than literature [16, 23]. This led to the different beam positions at the ruby. Measuring slightly from the centre causes a decrease in wavelength. Measurement 4 also contained an air bubble in the sample chamber and, therefore, did not transform into a crystal structure.

The glycerol-water mixtures shows an unexpected relationship between the Raman peaks of glycerol and water. Above 10 mol% the glycerol signal of the CH-2 stretch did not match expectations. This may have arisen from measurements at an inhomogeneous location.

Both measurements represent pre-experiments in view of an upcoming beamtime that will investigate the dynamics of glycerol at elevated pressures and low temperatures. Therefore, it would have been interesting to see glycerol and some solutions under pressure in the Raman spectrometer, but this could not be done because of the breaking of a diamond.

A. Appendix

A.1. Tables and figures

A.1.1. Sketches of components

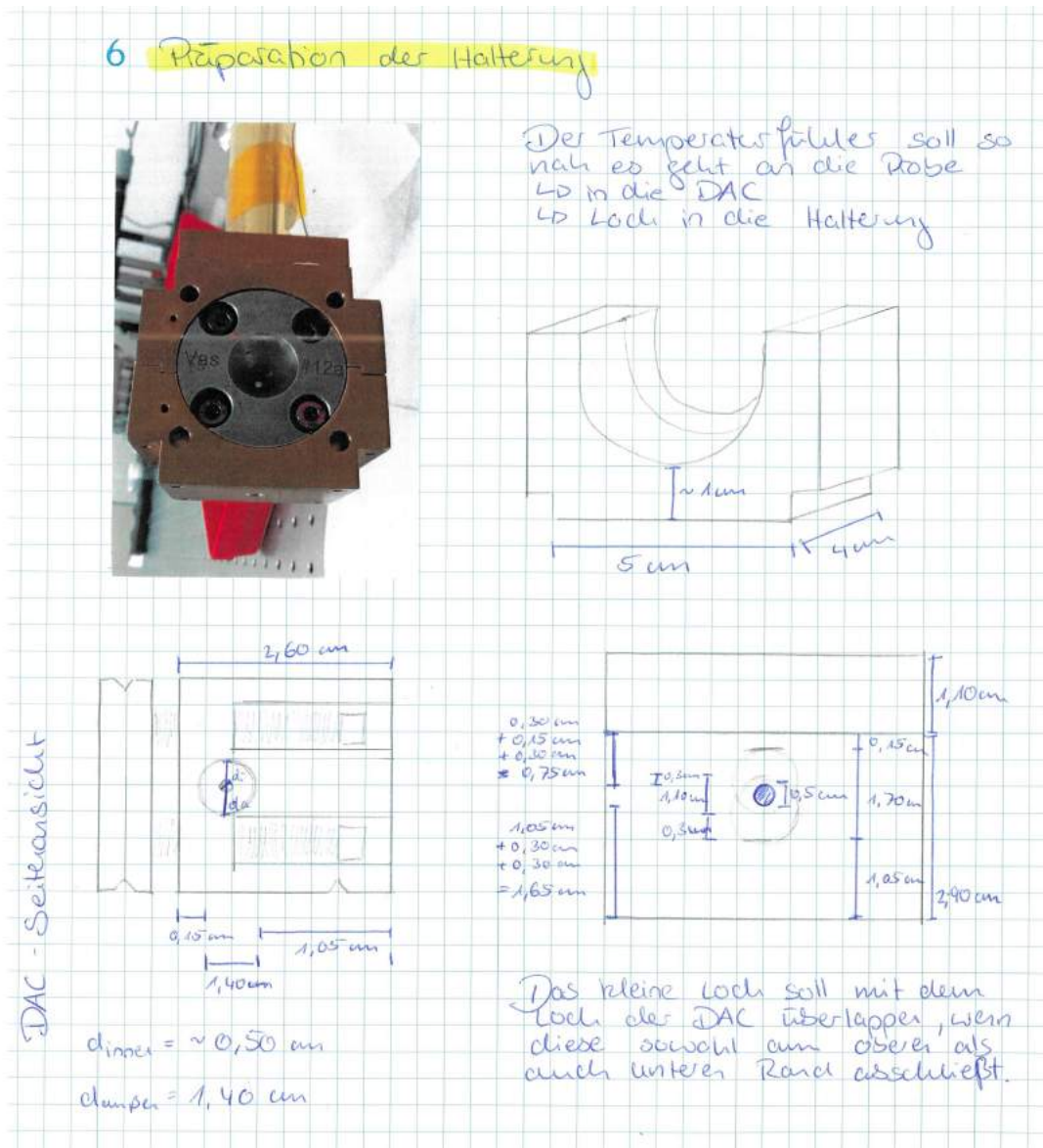


Figure A.1.: Extract from the laboratory book with the measurements of DAC I and the copper fitting. The upper left corner shows the finished fitting

A. Appendix

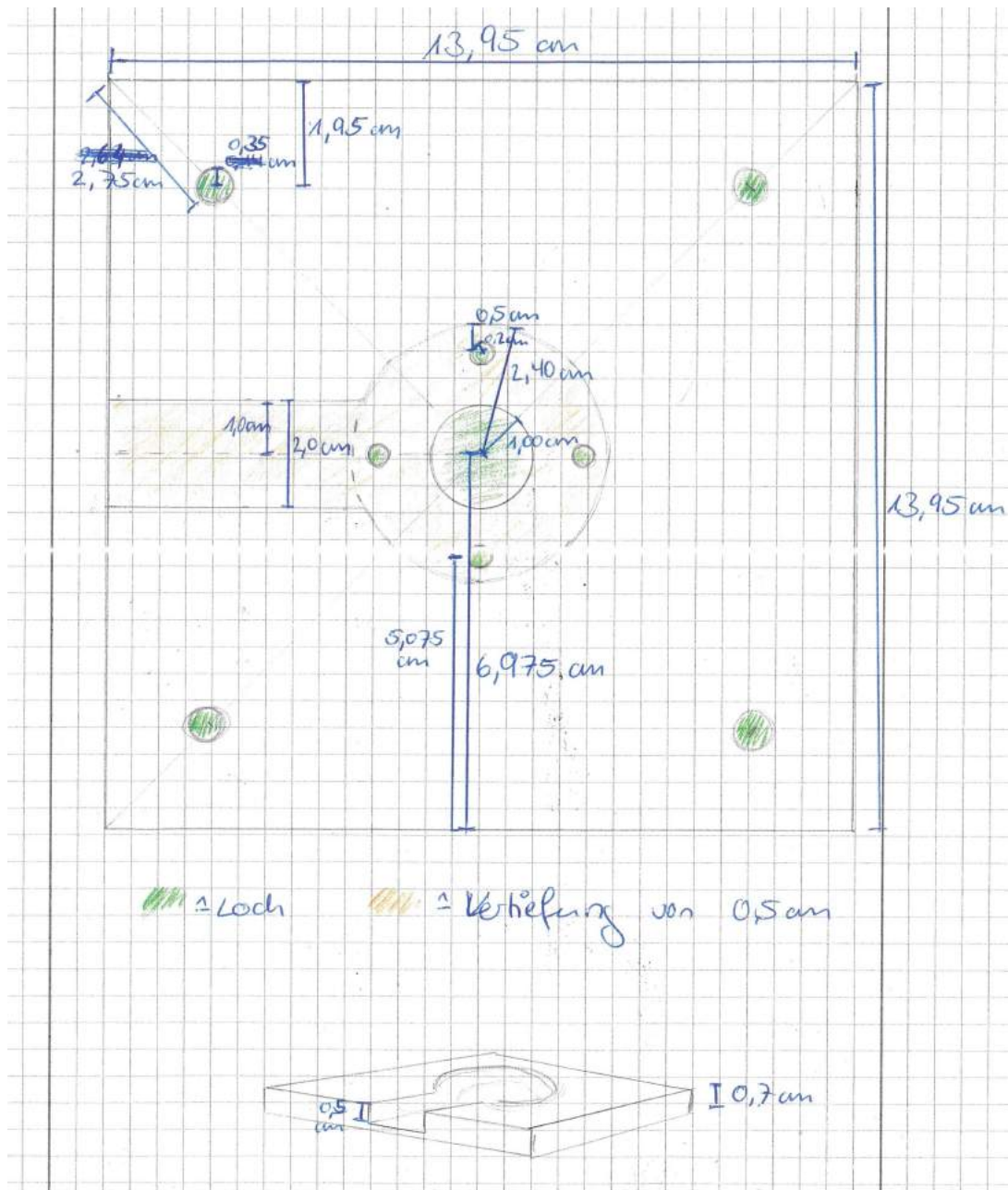


Figure A.2.: Copie of the sketch handed in to the workshop. Due to the material in the workshop, the plate has a thickness of 0.8 mm instead of 0.7 mm

A. Appendix

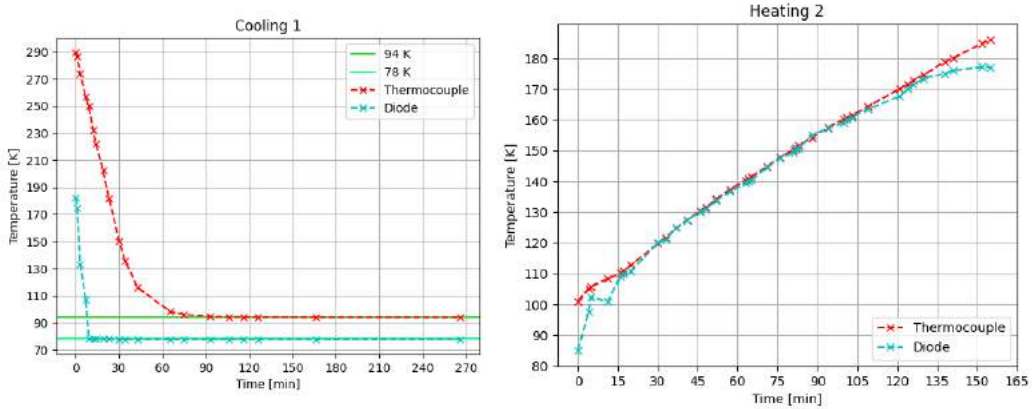


Figure A.3.: Left: Cooling process 1. The thermocouple (TC) took (97 ± 5) min longer to equilibrate than the diode
 Right: Heating process 2, without waiting for the TC to equilibrate.

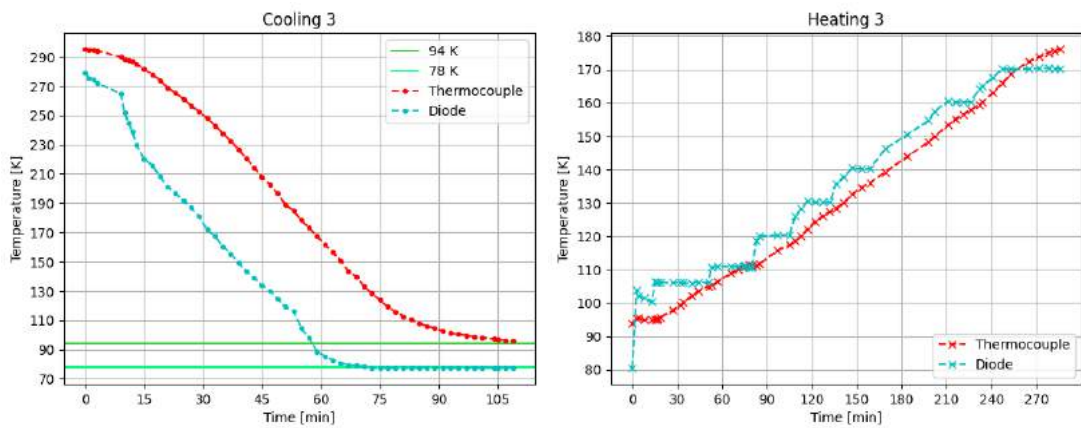


Figure A.4.: Cooling and Heating in measurement 3. The TC took (40 ± 5) min longer to equilibrate than the diode. But the measurement was interrupted at 96.03 K of the TC. The heating process was not measured til the TC was equilibrated.

A. Appendix

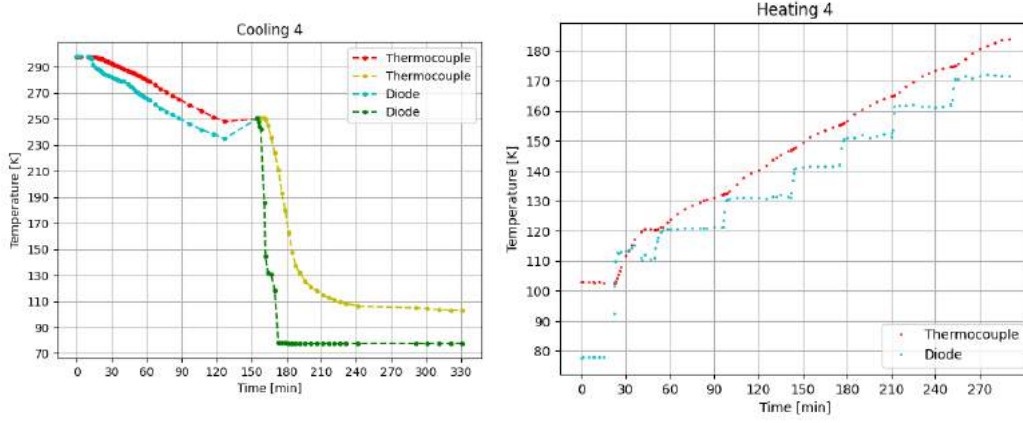


Figure A.5.: Cooling and heating process in measurement 4. In the first part of the cooling, the nitrogen tank was empty, so the measurement was interrupted after 130 min to refill.

A.1.2. Temperature calibration

Setpoint	Time	LakeShore	Thermocouple
100 K	17:00 - 17:25	100.5 K → 105.5 K → 102 K	104.15 K → 113.15 K
110 K	17:27 - 17:44	110 K → 111 K	115.15 K → 125.15 K
110 K	17:44 - 18:00	111 K → 112 K	125.15 K → 127.15 K
129 K	18:18 - 18:52	123.3 K → 122.3 K	134.35 K → 135.45 K

Table A.1.: Table of the temperature measurement by Aigerim Karine. Distance TC-Diode: ca. 5 mm, vacuum: 4×10^{-4} mbar to 6×10^{-4} mbar

A. Appendix

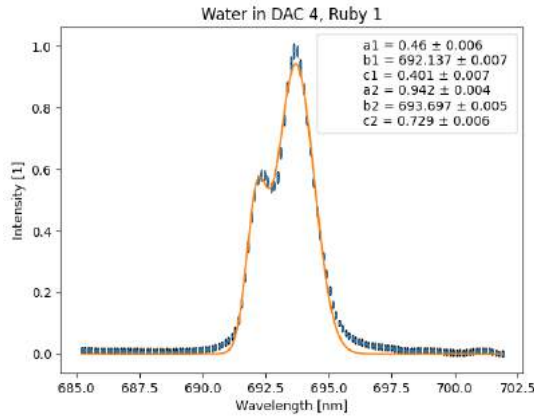
A.2. Raman measurements

A.2.1. Ruby spectra

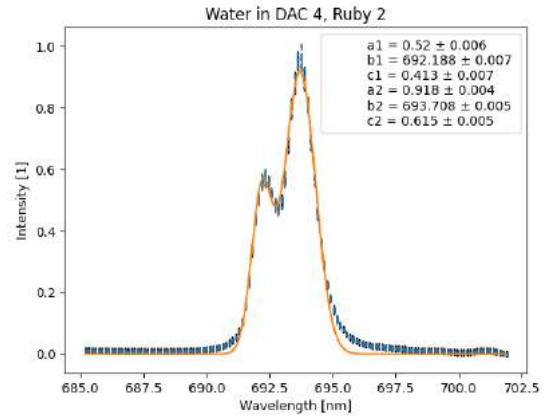
The ruby spectra are fitted to a gaussian double peak of the form

$$f(x) = a1 * \exp\left(-\frac{(x - b1)^2}{2 c1^2}\right) + a2 * \exp\left(-\frac{(x - b2)^2}{2 c2^2}\right) \quad . \quad (\text{A.1})$$

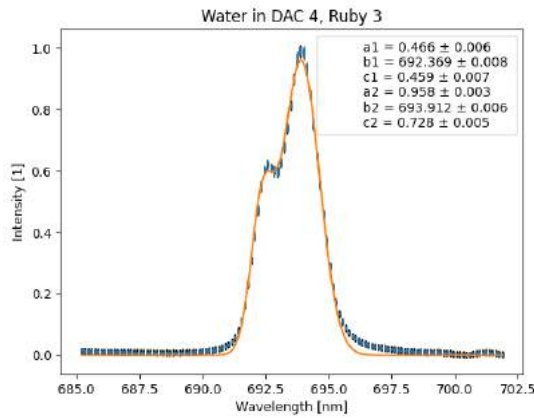
The parameters are plotted with the corresponding errors in the following.



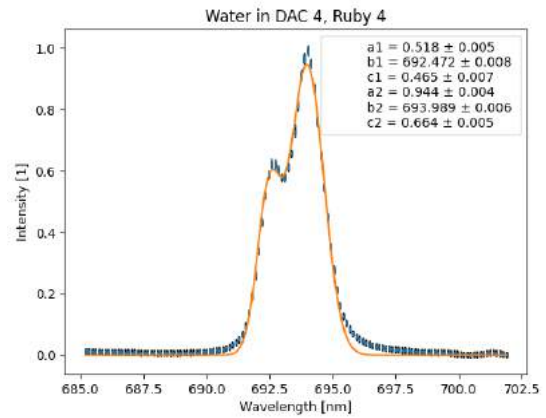
a) red. χ^2 : 4.437



b) red. χ^2 : 5.108

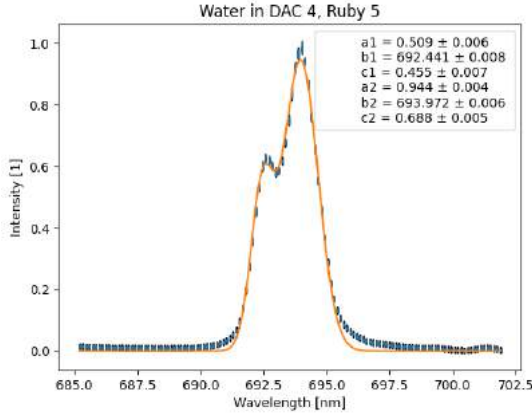


c) red. χ^2 : 3.032

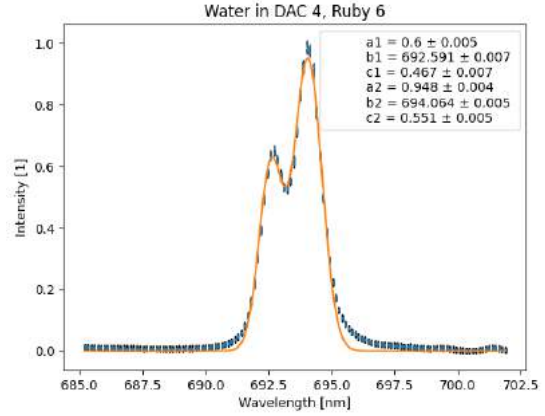


d) red. χ^2 : 3.666

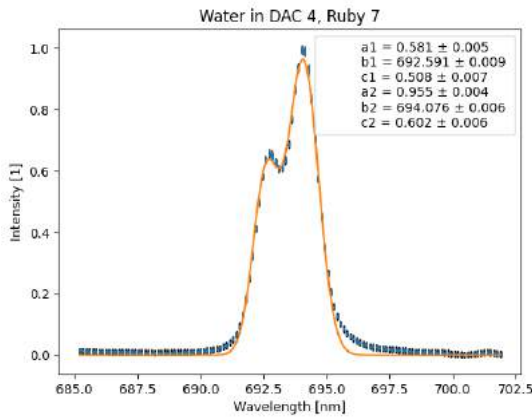
A. Appendix



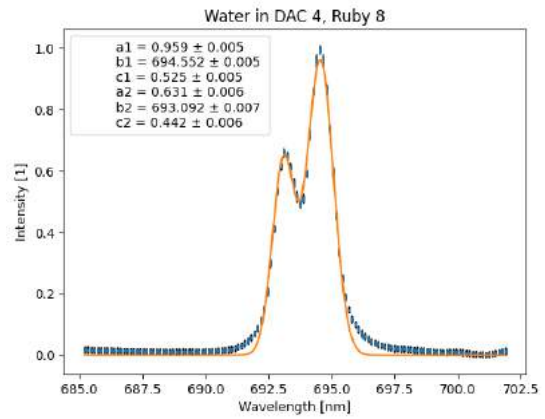
e) red. χ^2 : 3.657



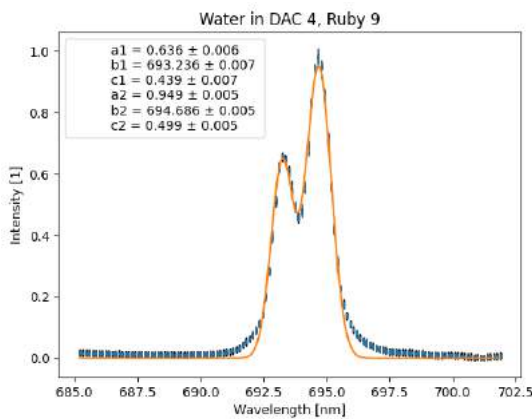
f) red. χ^2 : 4.544



g) red. χ^2 : 4.026



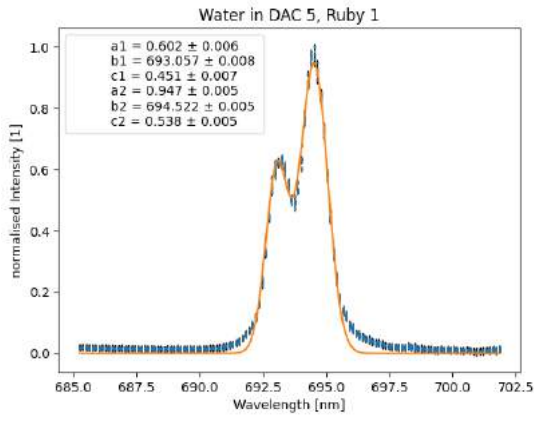
h) red. χ^2 : 5.812



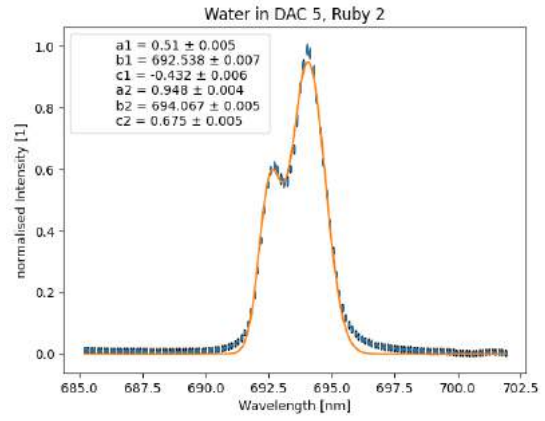
i) red. χ^2 : 6.341

Figure A.6.: Raman spectra of the ruby in measurement 4. The caption displays the reduced chi square of the corresponding Gaussian fit.

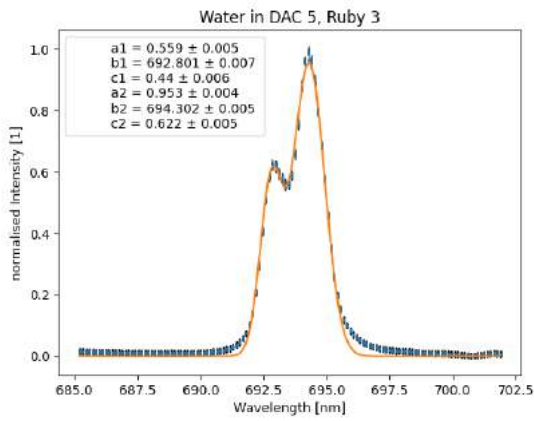
A. Appendix



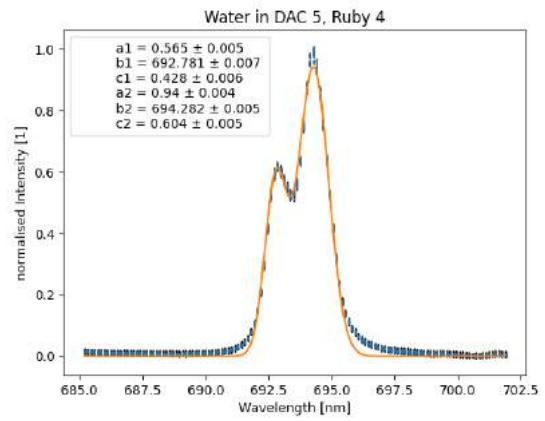
a) red. χ^2 : 6.069



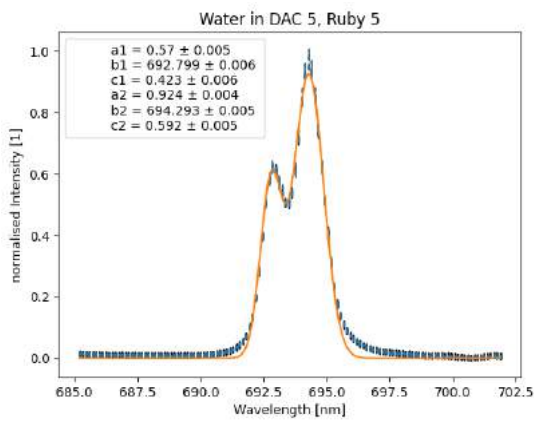
b) red. χ^2 : 3.586



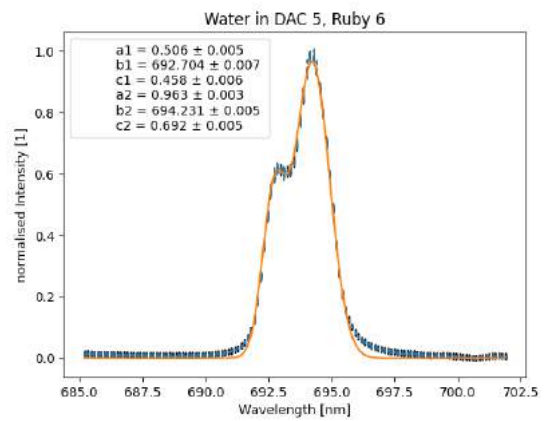
c) red. χ^2 : 3.876



d) red. χ^2 : 4.276

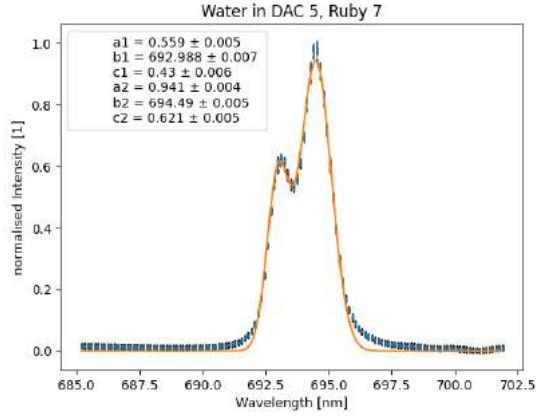


e) red. χ^2 : 4.355

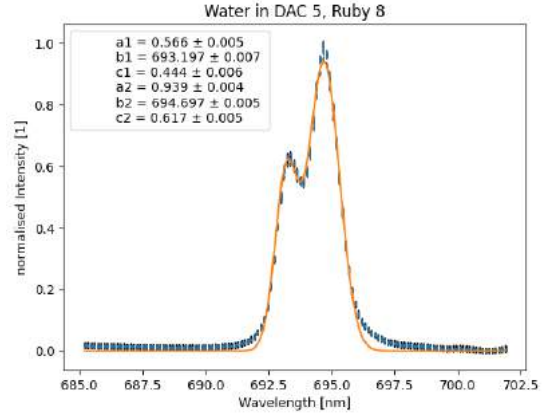


f) red. χ^2 : 2.792

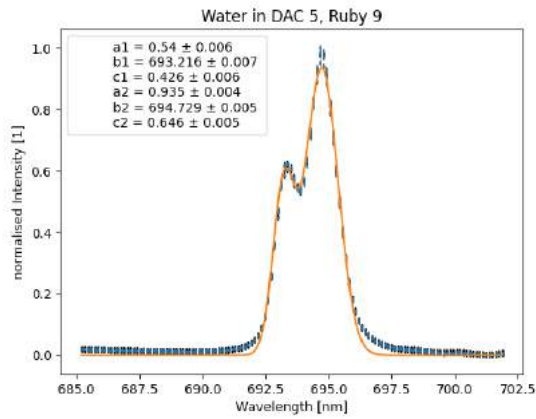
A. Appendix



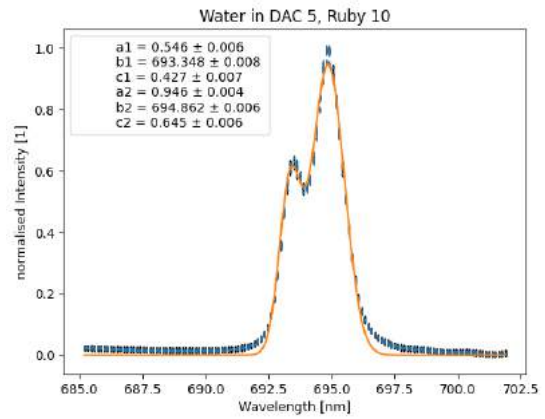
g) red. χ^2 : 4.286



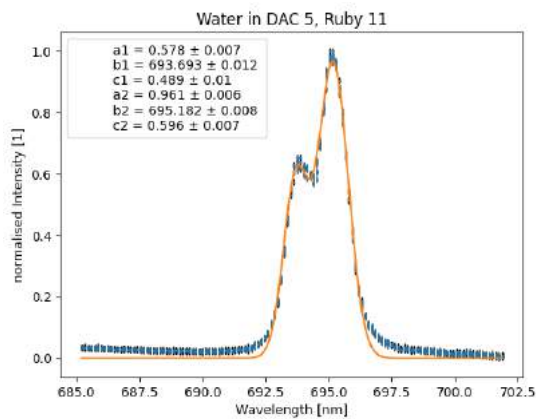
h) red. χ^2 : 4.275



i) red. χ^2 : 4.417



j) red. χ^2 : 5.240



k) red. χ^2 : 7.826

Figure A.7.: Raman spectra of the ruby in measurement 5. The caption displays the reduced chi square of the corresponding Gaussian fit.

A. Appendix

A.2.2. Glycerol mixtures

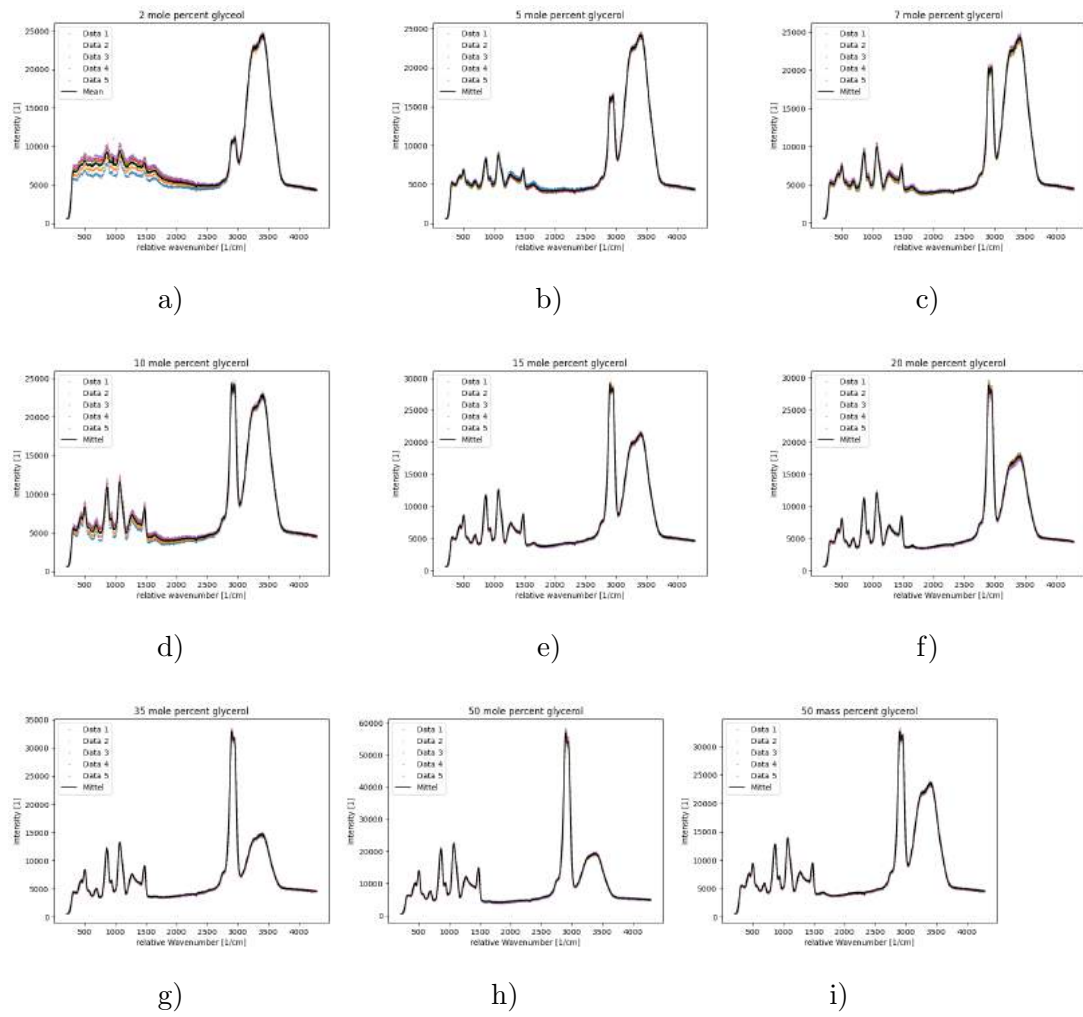


Figure A.8.: The data of the glycerol-water mixtures. All acquired at (5.0 ± 0.1) mW laser power and 60 s exposure time of each frame.

Bibliography

- [1] International association for the properties of water and steam, iapws g5-01(2020), guideline on the use of fundamental physical constants and basic constants of water, 2001.
as of 6.08.2023.
- [2] 2012.
URL https://commons.wikimedia.org/wiki/File:%3ADiamond_Anvil_Cell_-_Cross_Section.svg.
as of 01.08.2023.
- [3] Accurate crystal structure of ice vi from x-ray diffraction with hirshfeld atom refinement.
IUCrJ, 9:573–579, 2022.
ISSN 2052-2525.
URL <https://doi.org/10.1107/S2052252522006662>.
- [4] Muhtar Ahart, Dilare Aihaiti, Russell J. Hemley, and Seiji Kojima.
Pressure dependence of the boson peak of glassy glycerol.
J. Phys. Chem. B, (27):6667–6672, 2017.
URL <https://doi.org/10.1021/acs.jpcc.7b01993>.
- [5] C. A. Angell.
Liquid fragility and the glass transition in water and aqueous solutions, 2002.
URL <https://doi.org/10.1021/cr000689q>.
- [6] Johannes Bachler, Violeta Fuentes-Landete, David A. Jahn, Jessina Wong, Nicolas Giovambattista, and Thomas Loerting.
Glass polymorphism in glycerol–water mixtures: Ii. experimental studies.
Phys. Chem. Chem. Phys., 18:11058–11068, 2016.
URL <https://doi.org/10.1039/C5CP08069J>.
- [7] Reinhard Boehler and Koen De Hantsetters.
New anvil designs in diamond-cells.
High Pressure Research, 24(3):391–396, 2004.
URL <https://doi.org/10.1080/08957950412331323924>.
- [8] M. Chaplin.
Water structure and science., 2022.
URL https://water.lsbu.ac.uk/water/water_structure_science.html.
as of 16.07.2023.
- [9] F. Datchi, A. Dewaele, P. Loubeyre, R. Letoullec, Y. Le Godec, and B. Canny.

Bibliography

- Optical pressure sensors for high-pressure–high-temperature studies in a diamond anvil cell.
High Pressure Research, 27(4):447–463, 2007.
URL <https://doi.org/10.1080/08957950701659593>.
- [10] Wolfgang Demtröder.
Springer-Verlag GmbH Deutschland, Kaiserslautern, 7. korr. u. erw. aufl. edition, 2017.
- [11] Nakagawa H and Oyama T.
Molecular basis of water activity in glycerol-water mixtures.
Frontiers in chemistry, 7:731, Nov 1 2019.
URL <https://doi.org/10.3389/fchem.2019.00731>.
- [12] Klaus Irrgang.
Altes und Neues zu thermoelektrischen Effekten und Thermoelementen, volume 2.
Springer Vieweg Berlin, Heidelberg, 2023.
URL <https://doi.org/10.1007/978-3-662-66419-3>.
- [13] I. Kantor.
Flourescence presure calibration and thermocouple tools.
URL <http://kantor.50webs.com/ruby.htm>.
as of 01.08.2023.
- [14] Aigerim Karina.
Spectroscopic studies on phase transition in amorphous ices, 2022.
- [15] H. K. Mao, P. M. Bell, J. W. Shaner, and D. J. Steinberg.
Specific volume measurements of Cu, Mo, Pd, and Ag and calibration of the ruby R1 fluorescence pressure gauge from 0.06 to 1 Mbar.
Journal of Applied Physics, 49(6):3276–3283, 08 2008.
ISSN 0021-8979.
URL <https://doi.org/10.1063/1.325277>.
- [16] H. K. Mao, J. Xu, and P. M. Bell.
Calibration of the ruby pressure gauge to 800 kbar under quasi-hydrostatic conditions.
Journal of Geophysical Research: Solid Earth, 91(B5):4673–4676, 1986.
URL <https://doi.org/10.1029/JB091iB05p04673>.
- [17] Vadivel Masilamani, Hamid M. Ghaithan, Mamduh J. Aljaafreh, Abdullah Ahmed, Reem al Thagafi, Saradh Prasad, and Mohamad S. Alsalhi.
Using a spectrofluorometer for resonance raman spectra of organic molecules.
Journal of Spectroscopy, 2017:7, 2017.
URL <https://doi.org/10.1155/2017/4289830>.
- [18] Efraim Mendelovici, Ray L. Frost, and Theo Klopogge.
Cryogenic raman spectroscopy of glycerol.
Journal of Raman Spectroscopy, 31(12):1121–1126, 2000.
URL <https://doi.org/10.1002/1097-4555>.

Bibliography

- [19] Anoma Mudalige and Jeanne E. Pemberton.
Raman spectroscopy of glycerol/d₂o solutions.
Vibrational Spectroscopy, 45(1):27–35, 2007.
ISSN 0924-2031.
URL <https://doi.org/10.1016/j.vibspec.2007.04.002>.
- [20] M. Paluch, R. Casalini, S. Hensel-Bielowka, and C. M. Roland.
Effect of pressure on the relaxation in glycerol and xylitol.
The Journal of Chemical Physics, 116(22):9839–9844, 05 2002.
ISSN 0021-9606.
URL <https://doi.org/10.1063/1.1473652>.
- [21] Jürgen Popp and Thomas Mayerhöfer, editors.
Micro-Raman Spectroscopy, Theory and Application.
De Gruyter, Berlin, Boston.
URL <https://doi.org/10.1515/9783110515312>.
- [22] Jörn W.P. Schmelzer and Ivan S. Gutzow.
Glasses and the Glass Transition.
John Wiley Sons, Ltd, 2011.
URL <https://doi.org/10.1002/9783527636532>.
- [23] Guoyin Shen, Yanbin Wang, Agnes Dewaele, Christine Wu, Dayne E. Fratanduono, Jon Eggert, Stefan Klotz, Kamil F. Dziubek, Paul Loubeyre, Oleg V. Fat’yanov, Paul D. Asimow, Tsutomu Mashimo, Renata M. M. Wentzcovitch, and other members of the IPPS task group.
Toward an international practical pressure scale: A proposal for an ipps ruby gauge (ipps-ruby2020).
High Pressure Research, 40(3):299–314, 2020.
URL <https://doi.org/10.1080/08957959.2020.1791107>.
- [24] M Tanaka, G Girard, R Davis, A Peuto, and N Bignell.
Recommended table for the density of water between 0 °c and 40 °c based on recent experimental reports.
Metrologia, 38(4):301, aug 2001.
URL <https://dx.doi.org/10.1088/0026-1394/38/4/3>.
- [25] Alexander V. Thoeny, Tobias M. Gasser, and Thomas Loerting.
Distinguishing ice -xv from deep glassy ice vi: Raman spectroscopy.
Phys. Chem. Chem. Phys., 21:15452–15462, 2019.
- [26] Yasunori Tominaga, Aiko Fujiwara, and Yuko Amo.
Dynamical structure of water by raman spectroscopy.
Fluid Phase Equilibria, 144(1):323–330, 1998.
ISSN 0378-3812.
URL [https://doi.org/10.1016/S0378-3812\(97\)00276-8](https://doi.org/10.1016/S0378-3812(97)00276-8).
- [27] J. J. Towey and L. Dougan.
Structural examination of the impact of glycerol on water structure.

Bibliography

- The Journal of Physical Chemistry B*, 116(5):1633–1641, 2012.
URL <https://doi.org/10.1021/jp2093862>.
PMID: 22126327.
- [28] Xi Zhang, Peng Sun, Tingting Yan, Yongli Huang, Zengsheng Ma, Bo Zou, Weitao Zheng, Ji Zhou, Yinyan Gong, and Chang Q. Sun.
Water’s phase diagram: From the notion of thermodynamics to hydrogen-bond cooperativity.
Progress in Solid State Chemistry, 43(3):71–81, 2015.
ISSN 0079-6786.
URL <https://doi.org/10.1016/j.progsolidstchem.2015.03.001>.

Acknowledgements

At this point, I would like to thank Prof. Dr. Katrin Amann-Winkle for giving me the opportunity to write my bachelor's thesis in this wonderful research group, helping me with all my questions and for all her advice and corrections while writing this thesis. Thanks for all the opportunities, from gaining insights into the various facets of the Max Planck Institute to being involved in measurements at DESY.

A special thanks goes to Aigerim Karina, who introduced me to the diamond anvil cell and whom I could ask anything. Thanks to Christopher Ender for always opening the door to the Laboratory and to Jiaxu Liang for helping me find the right spectrometer settings. Furthermore, I would like to thank Sadeed Hameed, who prepared the glycerol-water solutions with me, and Louisa Kraft, who always helped me assemble the nitrogen setup.

Last but not least, I want to thank my roommate for supporting me during these studies with snacks and proofreading this thesis.